Gard Jonas Moen Gabrielsen

Comparison of Static Failure Criteria of Additively Manufactured Inconel 718 Analyzed by means of Strain Energy Density.

Master's thesis

NTNU
Norwegian University of Science and Technology
Faculty of Engineering
Department of Mechanical and Industrial Engineering

NTNU
Norwegian University of
Science and Technology

Gard Jonas Moen Gabrielsen

Comparison of Static Failure Criteria of Additively Manufactured Inconel 718 Analyzed by means of Strain Energy Density.

NTNU

Norwegian University of
Science and Technology

1 Preface

This master thesis was written spring 2019 as my final work in the two year master of science program of mechanical engineering at the department of mechanical and industrial engineering, Norwegian University of Science and Technology. This work serve as a continuation of my specialization project "Fatigue Behavior of Additively Manufactured Inconel 718 Analyzed by means of Strain Energy Density" during my previous semester supervised by Filippo Berto and Klas Solberg.

I want to thank them both for giving me good guidance, introducing me the strain energy density approach and for giving me freedom to shape my thesis topic. It has been enjoyable.

2 Abstract

As produced (AP) blunt V-notched and unnotched specimen of Inconel 718 (IN718) were additively manufactured (AM) by means of selective laser melting (SLM) and then statically tensile tested. Subsequently, the strain energy density (SED) of the notched specimen was computed with four different equations for sharp and blunt V-notches, using both elastic and plastic notch stress intensity factor (NSIF)(P-NSIF). Values of critical radii were determined by analytical, numerical and graphical methods. The failure accuracy was obtained using four different critical SED values. These values were computed employing brittle, ductile, linear elastic-perfectly plastic and perfectly plastic material models. When using the equation for blunt V-notches with NSIF and perfectly plastic failure criteria, the failure force was underestimated by 12.5%. The accuracy is comparable with elasto-plastic theory of critical distance (TCD), with reported deviation of $\pm12\%$, which is regarded as accurate. Nevertheless, the linear elastic SED approach can be recommended for estimation of both static and fatigue failure forces as less computationally demanding than TCD method. This stems from low mesh sensitivity in numerical analysis an the size effect of the NSIF. A new failure criterion was suggested based on analysis of material notch sensitivity ratio (NSR). However, further research needs to be conducted so as to verify the method and failure criterion by varying materials and geometries.

3 Sammendrag

En glatt prøvestav og prøvestav med butt V-kjerv av Inconel 718 (IN718) ble additiv produsert (AM) ved hjelp av selektiv lasersmelting (SLM) uten etterbehandling. Senere ble de statisk strekkprøvet. Styrken til prøvestaven med butt V-kjerv ble deretter estimert med fire forskjellige ligninger av strain energy density (SED) for skarpe og butte V-kjerver, ved bruk av både elastisk og plastisk kjervsensitivitets- og intensitetsfaktor (NSIF)(P-NSIF). Kritisk radius ble utledet ved hjelp av både analytisk, numerisk og ved grafisk metode. Nøyaktigheten ble sammenlignet ved bruk av fire forskjellige utledede kritiske SED-verdier. Disse var basert på en sprø, duktil, lineærelastisk-perfekt plastisk og et perfekt plastisk materialmodell. Materialmodelene var basert på materialegenskapene til den glatte prøvestaven. Nøyaktigheten ved å bruke ligningene for butt V-kjerv med NSIF var på 12.5% med feilkriteriet for det perfekt plastiske materialet. Nøyaktigheten er sammenlignbar med elasto-plastisk theory of critical distance (TCD) med rapportert feilmargin på ±12%. Imidlertid kan den lineære-elastiske SED-tilnærmingen bli anbefalt som en enkel måte å estimere statisk- og tretthetsbrudd. Dette skyldes lav følsomhet for størrelsen på mesh i de numerisk analysene og at størrelseseffekten er inkludert i NSIF. Et nytt feilkriterium med en inkludering av kjervfølsomhetsforholdet (NSR) ble foreslått. Men for å verifisere både fremgangsmåte og feilkriteriet må flere materialer og geomtrier bli testet.

Nomenclature

Symbol	Description	Units
α	Angle	Rad
ϵ	Engineering strain	-
ϵ_n	Strain until necking	-
ϵ_p	Plastic strain	-
ϵ_t	True strain	-
γ	Angle	Rad
μ	Notch opening angle parameter	-
ν	Poisson	-
ω	Stress angle referring to coordinate system	Rad
$\overline{W}$	Average strain energy density	$\frac{Nmm}{mm^3}$
ρ	Radius	mm
σ	Engineering stress	MPa
σ_θ	Stress according to figure 5.14	MPa
σ_m	Mean stress	MPa
σ_t	True stress	MPa
σ_y	Yield stress	MPa
σ_{uts}	Ultimate tensile stress	MPa
τ	Shear stress	MPa
A	Area	mm^2
A_0	Initial area	mm^2
F	Force	N
H	Strain hardening coefficient	MPa
I_e, I_p	Elastic and plastic stress integral	-
K_f	Notch sensitivity factor	-
K_i	Elastic stress intensity factor	$MPa^{1-\lambda}$

K_i^N	Elastic notch stress intensity factor	$MPa^{1-\lambda}$
K_t	Elastic stress concentration factor	-
K_{IC}	Fracture toughness	$MPa\sqrt{m}$
K_{ip}	Plastic stress intensity factor	MPa^s
K_{ip}^N	Plastic notch stress intensity factor	MPa^s
K_{th}	Fracture threshold stress intensity	$MPa\sqrt{m}$
l	Length	mm
l_0	Initial length	mm
m,q	Creep rate exponents	-
n	Strain hardening exponent	-
N_f	Cycles to failure	-
Q	Activation energy	J
R	Load ratio	-
R_0	Critical radius	m
W_C	Critical strain energy density	$\frac{Nmm}{mm^3}$
x	Distance	mm
a	Crack length	mm
A,b	Power law components	-
d	Average grain diameter	m
E	Young's modulus	MPa
f	Geometry function	-
G	Shear modulus	MPa
N	Cycles	-
q	Notch sensitivity factor	-
R	Load factor	-
r	Radius	m
s	Stress singularity for an elastoplastic material	-
T	Temperature	Kelvin
U	Strain energy	Nmm

Contents

4 Introduction

4.1 Background and motivation

The need for materials with greater strength at elevated temperatures escalated with the invention of the gas turbine and jet engine in the early nineteen hundreds. This industry needed stronger, lighter and more temperature resistant materials. This created a new class of alloys called superalloys. They consist of greater number of alloy elements than the previous alloys. Beside having a general content of nickel, the alloy compound ranges from five to ten other elements [1].

Inconel 718 (IN718) was introduced in the early 1960's [2]. It is a nickel-based super alloy that combines high creep strength with great resistance against oxidation and contrary to previous super alloys, also exhibiting great weldability [3] [4]. Ordinary steel alloys can not operate at more than approximately 50% of the absolute melting temperature (MT), but some nickel-based superalloys such as IN 718 can operate at an excess of 70% of the absolute MT. This is because of its two-phase equilibrium of γ/γ' which locks the dislocations [1]. This makes In718 popular in the aerospace industry and for other extreme conditions with complex design [3]. However it is difficult to produce by conventional production methods, with complex geometries desired [5].

Additive manufacturing (AM) is contrary to traditional manufacturing, adding material instead of removing. AM enables superior component complexity with large gains in topology optimization [6]. However, it needs further refinement because of the inherent flaws materials undergo during production [7]. These refinements are such as residual stresses, high surface roughness and porosity because of lack of fusion, reasons why AM often needs treatment after production.

Strain energy density (SED) is used as failure criteria for both brittle- and semi-brittle behavior [8]. It states that failure occurs when the strain energy density is equal to the critical energy, W_C. This method enables FE-analysis using very course mesh, contrary to other failure assessments [9]. Which is why it is considered as a powerful tool to asses failure of notched and welded components. However, SED analysis of static failure of notched materials are not substantially studied and predicting ductile failure often involves heavy elasto-plastic analysis.

4.2 Problem description

It is important to be able to accurately compute the failure force on components. Additive manufactured components enables more complex geometries than before, creating perturbations in the material acting. The strain energy density approach has been verified extensively for brittle and quasi-brittle material as a great prediction method of failure. This thesis investigates if it is possible to accurately predict static failure force of blunt V-notched specimen made of the ductile material Inconel 718.

4.3 Project scope

4.3.1 Objectives

The objective of this thesis is to determine the accuracy of the different computational methods.

4.3.2 Research questions

- What is the static mechanical properties of AM IN 718?

- Is it possible to give accurate estimations of static failure of AM IN 718 with blunt notch geometry, based on different linear calculation methods of the strain energy density criteria, with equations for sharp and blunt V-notches by use of NSIF and P-NSIF, when the failure criteria is based on brittle, ductile or simplified ductile materials?

4.3.3 Limitations

One material and one notch geometry limits the certainty of the conclusion of the method. Only Mode I load was considered.

4.4 Thesis structure

A chapter of literature review is included to provide some necessary knowledge of relevant topics. The review goes through stress, material response and static failure criteria. Further it contain other fatigue failure assessments, before introducing the theory of critical distance, the average strain energy density approach based on elastic NSIF as well as the equivalent strain energy density based on plastic P-NSIF. After which follows a brief intro to additive manufacturing, selective laser melting and hot isostatic pressing before giving a more extensive review of Nickel-based superalloys. This review includes mechanical properties of conventionally manufactured IN 718 as well as produced by additive manufacturing. The method of material testing are explained and how the strain energy density analysis was performed with numerical analysis, as well as the strain energy density approach in this thesis with all the necessary parameters for computation. Results of computed failure force and accuracy of the different methods are given, and these are discussed in the following chapter. The thesis ends with a conclusion and suggested further work.

5 Literature Review

5.1 Stress

Stress is the force applied divided by area [10]. When a component is subjected to a load it responds with a deflection, strain.

$$\sigma = \frac{dF}{dA}, \quad d\epsilon = \frac{dl}{l_0} \tag{1}$$

The stress tensor can in Cartesian coordinates be expressed as:

$$\sigma = \begin{bmatrix} \sigma_{11} & \sigma_{12} & \sigma_{13} \\ \sigma_{21} & \sigma_{22} & \sigma_{23} \\ \sigma_{31} & \sigma_{32} & \sigma_{33} \end{bmatrix}, \quad or \quad \sigma = \begin{bmatrix} \sigma_{11} & \tau_{12} & \tau_{13} \\ \tau_{12} & \sigma_{22} & \tau_{23} \\ \tau_{13} & \tau_{23} & \sigma_{33} \end{bmatrix} \tag{2}$$

With Cartesian coordinate system:
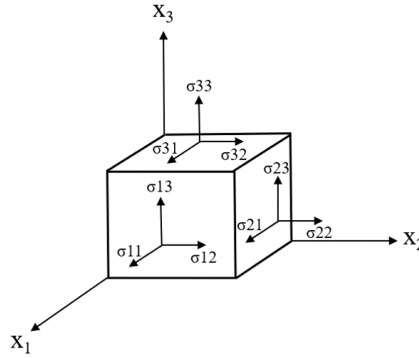
Figure 5.1: Illustrated stress tensors in Cartesian coordinates

5.2 Material response

The relation between stress and strain for isotropic materials in three dimensions is given in Hooke's law in equation 3.

$$\begin{bmatrix} \sigma_{11} \\ \sigma_{22} \\ \sigma_{33} \\ \sigma_{23} \\ \sigma_{13} \\ \sigma_{12} \end{bmatrix} = \frac{E}{(1+\nu)(1-2\nu)} \begin{bmatrix} 1-\nu & \nu & \nu & 0 & 0 & 0 \\ \nu & 1-\nu & \nu & 0 & 0 & 0 \\ \nu & \nu & 1-\nu & 0 & 0 & 0 \\ 0 & 0 & 0 & \frac{1-2\nu}{2} & 0 & 0 \\ 0 & 0 & 0 & 0 & \frac{1-2\nu}{2} & 0 \\ 0 & 0 & 0 & 0 & 0 & \frac{1-2\nu}{2} \end{bmatrix} \begin{bmatrix} \epsilon_{11} \\ \epsilon_{22} \\ \epsilon_{33} \\ 2\epsilon_{23} \\ 2\epsilon_{13} \\ 2\epsilon_{12} \end{bmatrix} \tag{3}$$

Strain can also be affected by changes of temperature, which effects the amount of vibration of the atoms in the solid. The effect is equally large in all directions in an isotropic material, and is proportional with the temperature change ΔT, this is given in the equation (4).

$$\epsilon = \alpha(T - T_0) = \alpha(\Delta T) \tag{4}$$

We differ from engineering stress σ and true stress σ_t, and thereby also of engineering strain ϵ and true strain ϵ_t.

$$\sigma = \frac{F}{A_0}, \quad \sigma_t = \sigma(1+\epsilon), \quad \epsilon = \frac{l-l_0}{l_0}, \quad \epsilon_t = ln(1+\epsilon). \tag{5}$$

Mechanical strength properties is often extracted from monotonic stress-strain tensile tests. Materials will either exhibit behavior from, or in between brittle to ductile manner as seen under in figure 5.2.
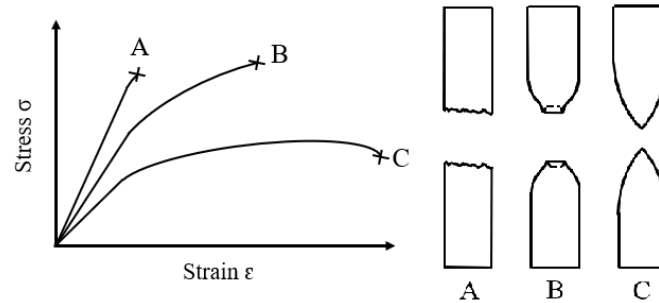

Figure 5.2: Different material response. A: Brittle, B: Partly ductile and C: Ductile behavior.

Yield strength σ_y is defined as the largest stress before deforming plastically. This is where the material will return to its original shape when removing the applied load. Often materials don't have an easily defined yield point, instead the offset yield strength is defined as the limit which give an strain of 0.2% often called $R_{p0.2}$ or σ_O. The linear relationship between stress and strain below the yield strength is the modulus of elasticity, or Young's modulus ($\sigma = E\epsilon$). Shear modulus is the ratio of shear stress to shear strain denoted often as $G = \frac{\tau_{xy}}{\gamma_{xy}}$. Ultimate tensile strength σ_{uts} is the greatest engineering stress the material can withhold, before we reach stress at failure σ_f, shown in figure 5.3. ¨
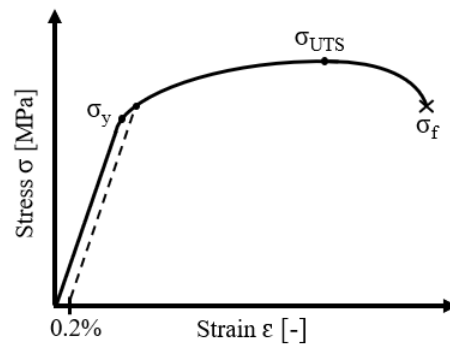

Figure 5.3: Stress-strain curve showing different material strengths

Plastic deformation of materials happens after exceeding the yield strength. Often it does not result in a significant change in volume, contrary to elastic deformation which does when the Poisson's ratio is less than 0.5. The plasticity is determined by different mechanisms such as dislocations, which travel through the lattice even at low stress but is rapidly growing in numbers when exceeding the yield limit.

The Ramberg-Osgood relation assumes that plastic stress is proportional to the plastic strain raised to a power [11]. It is therefor applied beyond the yield strength σ_y, with the elastic strain being proportional to stress according to $\epsilon_e = \sigma/E$.

$$\sigma = H\epsilon_p^n, \qquad \epsilon_p = \epsilon - \frac{\sigma}{E}. \tag{6}$$

H is the strain hardening constant and n is the strain hardening exponent. The plastic strain, $\epsilon_p = \epsilon - \frac{\sigma}{E}$, is the strain that deviates from the slope of the elastic modulus E. The total strain can be given as:

$$\epsilon = \frac{\sigma}{E} + \left(\frac{\sigma}{H}\right)^{\frac{1}{n}} \tag{7}$$
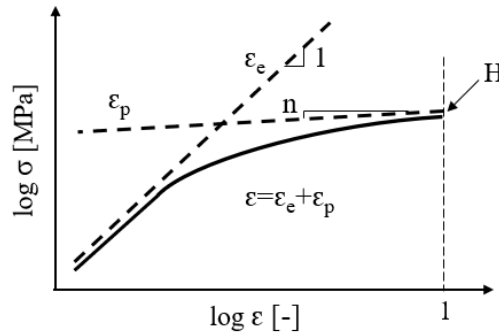
Figure 5.4: The Ramberg-Osgood relationship.

Beside elastic and plastic deformation, materials also undergo a time-dependent deformation behavior, called creep. Different types of physical mechanisms occur, but is in general divided into two different classes, diffusional flow and dislocation creep. Sometimes also grain boundary sliding is considered to be a distinct mechanism. Steady state creep rate can be calculated for crystalline materials by the equation:

$$\dot{\epsilon} = \frac{A_2 \sigma^m}{d^q T} \exp^{\frac{-Q}{RT}} \tag{8}$$

d is the average grain diameter, T the absolute temperature. A_2, the exponents m and q, and the activation energy Q depends on the material and which creep mechanism that is dominant. Creep is heavily influenced by temperature, indicating that the mechanisms are thermally activated.

5.2.1 Failure Criteria

Different failure criterion's exits. Two of the most widely used are the octahedral shear stress yield criterion and the maximum shear stress yield criterion. They are graphically compared in figure 5.5, where it is evident that the maximum shear criterion, or Tresca, is more conservative than the octahedral criterion (also known as von Mises).
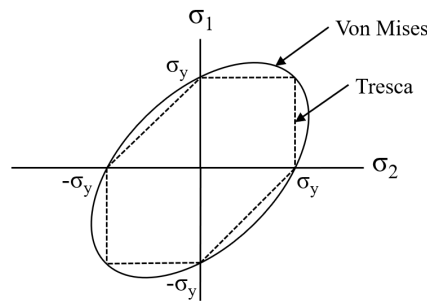
Figure 5.5: Graphical comparison of Von Mises- and Tresca criterion, with $\sigma_3 = 0$.

These criterion's are used both for static and fatigue failure assessment, primarily with the use of safety factors which often range from $1.5 - 3.0$, depending on the amount of uncertainty in the engineering assessment.

5.2.2 Fracture toughness

The material property K is a measure of the severity of a combination of crack length and shape, geometry and load. The materials resistance to brittle fracture with the presence of this crack is called the fracture toughness, K_{IC}, obtained from where the material fails, see figure 5.7. Figure 5.6 shows the different crack load modes, giving different crack intensity. They are separated into different modes for mechanical reason but real components often show mixed mode loading.
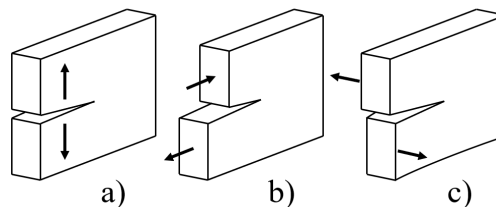

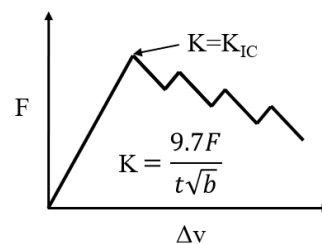Figure 5.6: a) Mode I, tension, b) Mode II, shear, c) Mode III, tear.

Figure 5.7: Fracture toughness test with specimen dimensions equal to 5.11 b).

5.3 Fatigue

Fatigue is when a material is subjected to an alternating load until failure [10]. A typical measure of fatigue limit is numbers of cyclic loads before failing, with either stress or strain response. Many factors control the fatigue limit of components such as, material properties, geometry, size effect, surface roughness, environment etc. The mean stress σ_m is also determining for the fatigue limit. This is because of inherent flaws in the material which make the material weaker in tensile fatigue load. In compressive loads, the flaws does not have the same effect. Fatigue parameters of stress are shown in the figure 5.8 below, with explanation in equation 9.
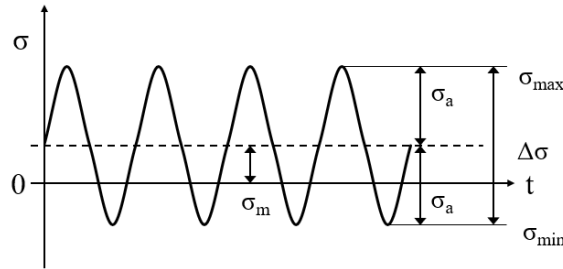

Figure 5.8: Parameters of a stress cycle.

Fatigue parameters of describing the cyclic loads are given as:

$$\Delta\sigma = \sigma_{max} - \sigma_{min}, \quad \sigma_a = \frac{\Delta\sigma}{2}, \quad \sigma_m = \frac{\sigma_{max} + \sigma_{min}}{2}, \quad R = \frac{\sigma_{min}}{\sigma_{max}} \tag{9}$$

The mean stress effect can be incorporated into the fatigue equations in the two next chapters.

5.3.1 Stress based approach

A stress versus cycle curve or S-N diagram is often used to design components, where life of specimens are dominated by crack initiation. Tests are usually run until components reach life of 10^7 cycles. This is to cover conventional life spans of components and for time limiting factors. Lower stress amplitude gives in general greater scatter of life expectancy. Many material exhibit a linear trend of the fatigue lives when plotting the fatigue data in a S-N diagram. This linear trend can be fitted to the Basquin equation in 10 with explanation in figure 5.9 [12].

$$\frac{\Delta\sigma}{2} = \sigma'_f(N_f)^b \tag{10}$$

Some materials will exhibit an "endurance limit" where the material will not fail below. A low probability of fracture is obtained by applying a safety factor. Life span of real components can be predicted by introducing life limiting factors. These can easily be multiplied the fatigue data obtained.
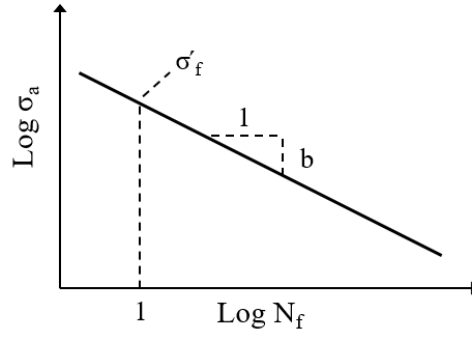
Figure 5.9: Basquin fit

The effect of a notch is predicted by modifying the unnotched fatigue data with a factor K_f. This sometimes differ from the elastic stress concentration factor K_t. Where K_t is the maximum stress of the notch root divided by the nominal stress, whereas K_f is the average stress over a finite volume.

$$K_f = 1 + q(K_t - 1) \tag{11}$$

The factor q determines the notch sensitivity of the material, 1 indicating fully notch sensitive and 0 no sensitivity. Neuber developed an approximation for determining the notch sensitivity factor for load factor of $R = -1$, with ρ being a material factor and the radius of the notch given as r [13].

$$q = \frac{1}{1 + \sqrt{\frac{\rho}{r}}} \tag{12}$$

While Peterson had developed a similar approach with the same load factor, where a is a different material factor [14].

$$q = \frac{1}{1 + \frac{a}{r}} \tag{13}$$

These approximations were developed because of the difficulties of describing the linear-elastic stress fields in the vicinity of the notch root or other stress risers. Peterson also observed that his approach at describing the notch fatigue sensitivity could not be recommended when dealing with small stress riser radii.

5.3.2 Strain based approach

A components deflections with an alternating load can be illustrated in a Hysteresis loop, were the material undergo plastic deformation and is either weakened or strengthened. The Coffin-Manson law describes the plastic LCF with constant strain amplitude [15], while the Basquin law in equation 10 describes the elastic part of fatigue regards to stress amplitude.

$$\frac{\Delta \epsilon}{2} = \frac{\Delta \epsilon_e}{2} + \frac{\Delta \epsilon_p}{2} \quad \rightarrow \quad \frac{\Delta \epsilon}{2} = \frac{\sigma_f'}{E}(2N_f)^b + \epsilon_f'(2N_f)^c \tag{14}$$
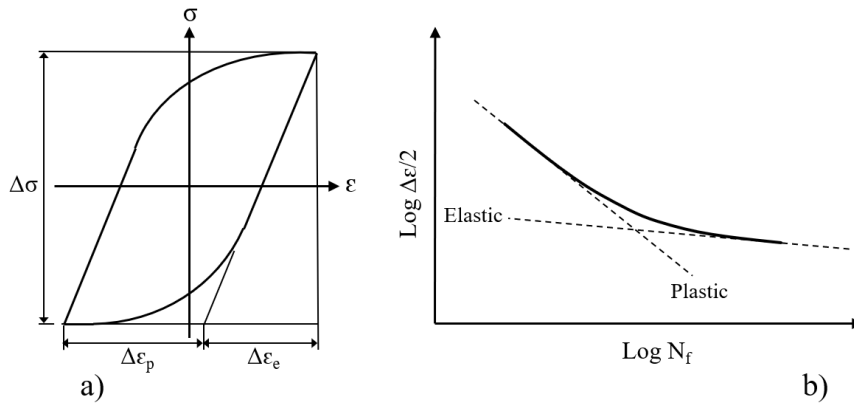
8

Figure 5.10: a) Hysteresis loop. b) Plastic and elastic dominated parts of fatigue.

5.3.3 Fracture mechanics

Fracture mechanics asses fatigue based on crack propagation [16]. The crack in this theory is initiated early in the cyclic life of an component and propagate until instability or failure. The crack is initiated at the threshold stress intensity, ΔK_{TH}, in which represents a stress intensity where cracks will not propagate below. The linear trend fit of the crack propagation in a log-log form can be approximated using Paris law in equation 15.
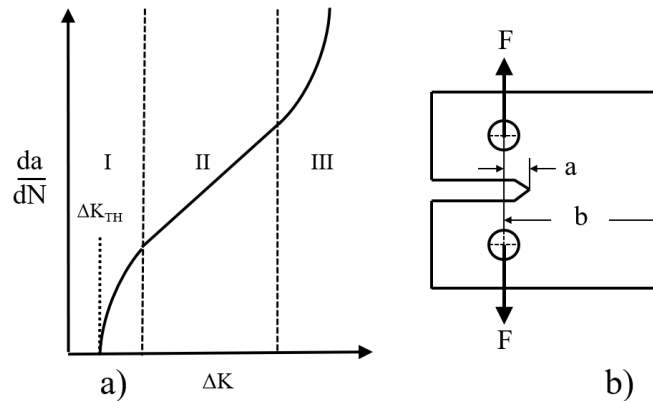
Figure 5.11: a) Crack growth rate in log-log coordinates. b) Test specimen design for crack length a.

K is determined by the stress and geometry factor f, the stress and crack length. The geometry factor is determined according to the shape of the test specimen, with an example shown in figure b) 5.11.

$$\frac{da}{dN} = C(\Delta K)^m, \quad \Delta K = \Delta\sigma\sqrt{\pi a}f \tag{15}$$

5.4 Theory of Critical Distance

The theory of critical distance (TCD) was invented in the early part of the 1900's century by Neuber to predict the strength of notched members [13]. His attempt to create a formal theory was based on the idea that the stress of the vicinity of the notch do not reach the values predicted in continuum mechanics theory. At that time the knowledge about the stress field in the vicinity of the notch was low, which made Neuber develop empirical models. But the combined use of TCD with modern FEM analysis of the stress field, gives an accurate method for fatigue [17] and static failure assessment [18]. The theory is based on a material length scale seen in equation 16.

$$L = \frac{1}{\pi} \left(\frac{K_{IC}}{\sigma_{ref}} \right)^2 \tag{16}$$

Where K_{IC} is the plain strain fracture toughness of the given material and σ_{ref} is a material reference strength experimentally derived. This reference strength is in cases of brittle materials similar to the ultimate tensile strength [19]. But in other materials exhibiting miner plasticity greater than it [17]. It is useful to show the relative link between LEFM and TCD:

$$\sigma_f = \frac{K_{Ic}}{\sqrt{\pi a}} \tag{17}$$

$$\sigma(r) = \sigma \sqrt{\frac{a}{2r}} \tag{18}$$

Equation 18 is only valid for a being infinitely larger than r. If combining these two equations with the PM criterion we get equation 16.

The traditional theory of critical distance consist of three fundamental approaches with the difference being how to define the failure stress σ_{eff}. The simplest of the approaches is the point method (PM), which Peterson formulated not long after Neuber's line method [14]. This approach states that the σ_{eff} is determined at a point half of the critical distance from the notch root as seen in figure 5.12. When the reference strength is greater than the ultimate tensile strength, it can be estimated as shown in the figure 5.12 below by using the point method by Peterson.
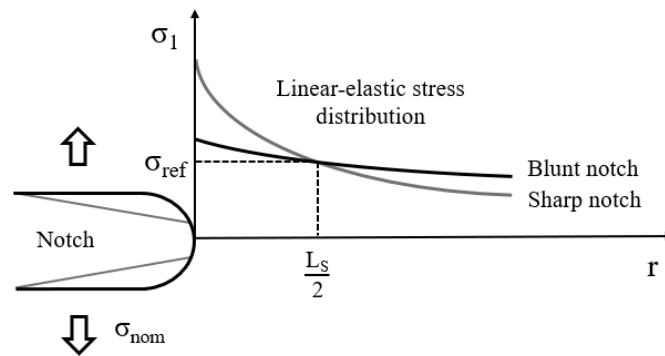

Figure 5.12: Stress versus distance curve with two different notch radii. σ_{eff} is experimentally derived using numerical analysis.

Peterson evaluated the critical length based on empirical values, fitting fatigue predictions to obtained material data. But he saw a possible correlation between the the critical distance and the inverse of the material strength of a particular class of materials, such as steels [14].

$$\sigma_{eff} = \sigma_1(r = \frac{L}{2}, \theta = 0) = \sigma_{ref} \tag{19}$$

Neuber invented the method called line method [13]. He overcome the problem of material inhomogeneity by averaging the classical theory over a length of a structural particle starting from the notch root, $2L$.

$$\sigma_{eff} = \frac{1}{2L} \int_0^{2L} \sigma_1(r, \theta = 0) dr = \sigma_{ref} \tag{20}$$

The area- and volume method are not commonly used, mainly because PM and LM reportedly gives accuracy in the same range but involve less complicated calculations.

$$\sigma_{eff} = \frac{4}{\pi L^2} \int_{-\frac{\pi}{2}}^{\frac{\pi}{2}} \int_0^L \sigma_1(r, \theta) dr d\theta \approx \sigma_{ref} \tag{21}$$

5.4.1 TCD in high-cycle fatigue

TCD are good methods of approximating HCF, with an usual 20% of in the conservative range compared to experimental results [17]. Susmel et al. [20] made successful modifications to approximate fatigue in the medium cycle fatigue area (MCF). In fatigue assessments, the ultimate tensile strength is changed with the plain fatigue limit $\Delta\sigma_0$, and the range of the threshold value for the stress intensity factor ΔK_{th} [21].

$$L = \frac{1}{\pi} \left(\frac{\Delta K_{th}}{\Delta\sigma_0} \right)^2 \tag{22}$$

And the fatigue limit for notched components is reached when the effective stress $\Delta\sigma_{eff}$, which depends on the stress distribution in the close vicinity of the notch tip, equals $\Delta\sigma_0$.

$$\Delta\sigma_{eff} = \Delta\sigma_0 \tag{23}$$

With the line method of predicting fatigue equals to:

$$\Delta\sigma_{eff} = \frac{1}{2L} \int_0^{2L} \Delta\sigma_1(r, \theta = 0) dr = \Delta\sigma_0 \tag{24}$$

Lazzarin et al. [22] argued that the line method should be corrected by using an a-dimensional function depending on length scale L and the notch root radius, r_n, formulated as:

$$\Delta\sigma_{eff} = \Delta\sigma_1(r = L, \theta = 0) \frac{1 + \sqrt{2}\frac{L}{r_n}}{1 + \frac{L}{r_n}} \tag{25}$$

11

5.5 Strain Energy Density

Strain energy is the energy stored in materials undergoing elastic or plastic deformation. Strain energy denoted as U can be expressed by.

$$U = \frac{1}{2} \int_V \sigma_{ij} \epsilon_{ij} dV \qquad (26)$$

Strain energy density (SED) criteria states that failure occurs when it reaches a critical value $\overline{W} = W_C$ [23]. The critical strain energy density can be calculated for brittle behavior by using the ultimate tensile strength σ_{UTS} in the relation $W_C = \sigma_{UTS}^2/2E$. The SED volume, and thereby also the distance R_0 is determined by the material properties. This distance differ in static and dynamic loads. The critical volume is shown in figure 5.13 below for a crack and notches.
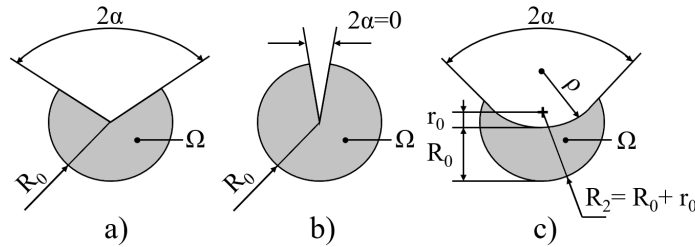
Figure 5.13: Mode I load. a) sharp V-notch. b) A crack. c) Critical volume for blunt V-notch [8]

In blunt notches there is a distance between the origin of the coordinate system and the notch root, see figure 5.14. The strain energy volume is defined by using Lazzarin's stress fields with an auxiliary coordinate system. This make it more efficient to impose the boundary conditions of the stress field [24].
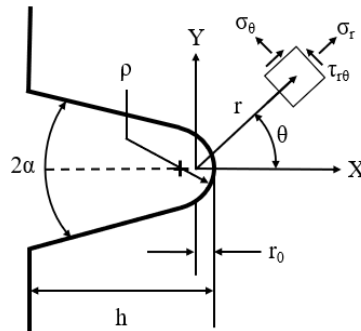

Figure 5.14: Coordinate system for the notch system with symbols used for the stress field components. $r_0 = \rho((\pi - 2\alpha)/(2\pi - 2\alpha))$.

The stress components of the stress field can according to LEFM be linked to a field parameter in such a way that when the notch opening angle and notch radius is zero, the parameters will be equal to the stress intensity factors. This means the definitions made by Gross [25] for open cracks is applicable in equa-

tion 27. Load Mode is shown in figure 5.6.

$$K_1 = \sqrt{2\pi} \lim_{r \to 0} (\sigma_\theta)_{\theta=0} r^{1-\lambda_1}, \quad K_2 = \sqrt{2\pi} \lim_{r \to 0} (\tau_{r\theta})_{\theta=0} r^{1-\lambda_2}. \tag{27}$$

K_i is the stress intensity factor, crack stress intensity factor (SIF) for an opening angle of $2\alpha = 0$, or notch stress intensity factor (NSIF) when $2\alpha > 0$.

$$a_1 = \frac{K_1}{\lambda_1 \sqrt{2\pi}[(1+\lambda_1) + X_1(1-\lambda_1)]}, \quad a_2 = \frac{K_2}{\lambda_2 \sqrt{2\pi}[(1-\lambda_2) + X_2(1+\lambda_2)]}. \tag{28}$$

The stress field for mode 1, or pure tensile stress can be calculated by using equation (29) and (30). (See Appendix).

$$
\begin{bmatrix} \sigma_\theta \\ \sigma_r \\ \tau_{r\theta} \end{bmatrix} = \frac{1}{\sqrt{2\pi}} \frac{r^{\lambda_1-1} K_1}{(1+\lambda_1) + X_1(1-\lambda_1)} \left[\begin{bmatrix} (1+\lambda_1)\cos(1-\lambda_1)\theta \\ (3-\lambda_1)\cos(1-\lambda_1)\theta \\ (1-\lambda_1)\cos(1-\lambda_1)\theta \end{bmatrix} \right.
$$
$$
+ X_1(1-\lambda_1) \begin{bmatrix} \cos(1+\lambda_1)\theta \\ -\cos(1+\lambda_1)\theta \\ \sin(1+\lambda_1)\theta \end{bmatrix} \tag{29}
$$
$$
\left. + \left(\frac{r}{r_0}\right)^{(\mu_1-\lambda_1)} [(3-\lambda_1) - X_1(1-\lambda_1)] \begin{bmatrix} \cos(1+\lambda_1)\theta \\ -\cos(1+\lambda_1)\theta \\ \sin(1+\lambda_1)\theta \end{bmatrix} \right]
$$

And for shear force, Mode II:

$$
\begin{bmatrix} \sigma_\theta \\ \sigma_r \\ \tau_{r\theta} \end{bmatrix} = \frac{1}{\sqrt{2\pi}} \frac{r^{\lambda_2-1} K_2}{(1-\lambda_2) + X_2(1+\lambda_2)} \left[\begin{bmatrix} -(1+\lambda_2)\cos(1-\lambda_2)\theta \\ -(3-\lambda_2)\cos(1-\lambda_2)\theta \\ (1-\lambda_2)\cos(1-\lambda_2)\theta \end{bmatrix} \right.
$$
$$
+ X_2(1+\lambda_2) \begin{bmatrix} -\sin(1+\lambda_2)\theta \\ \sin(1+\lambda_2)\theta \\ \cos(1+\lambda_2)\theta \end{bmatrix} \tag{30}
$$
$$
\left. + \left(\frac{r}{r_0}\right)^{(\mu_2-\lambda_2)} [(1-\lambda_2) + X_2(1+\lambda_2)] \begin{bmatrix} \sin(1+\lambda_2)\theta \\ -\sin(1+\lambda_2)\theta \\ -\cos(1+\lambda_2)\theta \end{bmatrix} \right]
$$

The parameters, λ_i, μ_i and X_i are dependent on the notch opening angle 2α and are listed in table 14. The critical radius of static load, R_{0s}, is analytically determined using Poisson's ratio, ultimate tensile strength and the fracture toughness. Depending on plane strain or plain stress condition it is calculated either by equation (31) or by equation (32) [26].

$$R_{0s} = \frac{(1+\nu)(5-8\nu)}{4\pi} \left(\frac{K_{IC}}{\sigma_{UTS}}\right)^2 \quad \text{plane strain} \tag{31}$$

$$R_{0s} = \frac{(5-3\nu)}{4\pi} \left(\frac{K_{IC}}{\sigma_{UTS}}\right)^2 \quad \text{plane stress} \tag{32}$$

Plane strain condition is when the fracture toughness is lower than the value defined in equation (33). Where B is the specimen thickness and σ_y the yield strength [27].

$$K_{Ic} = \sigma_y \left(\frac{B}{2.5} \right)^{\frac{1}{2}} \quad \text{plane strain} \tag{33}$$

While plane stress condition is when the fracture resistance is higher than that of K_{IC} in equation (34) [27].

$$K_{Ic} = \sigma_y (\pi B)^{\frac{1}{2}} \quad \text{plane stress} \tag{34}$$

An interpolation is needed to determine R_0 from equation (31) and (32) if the condition is between plane strain (33) and plane stress (34). Under plane stress or plane strain conditions, the elastic strain energy density averaged over a small sector with radius R_0 is given in equation 35. It is valid only when considering the first leading therms of the William's solution for sharp V-notches [23].

$$\overline{W} = \frac{1}{E} \left(e_1 \left[\frac{K_1}{R_{0s}^{1-\lambda_1}} \right]^2 + e_2 \left[\frac{K_2}{R_{0s}^{1-\lambda_2}} \right]^2 \right) \tag{35}$$

When the Poisson's ratio is equal to $v = 0.3$, the e_1 and e_2 becomes [23]:

$$e_1 = -5.373 \cdot 10^{-6} \cdot (2\alpha)^2 + 6.151 \cdot 10^{-4} \cdot (2\alpha) + 0.1330 \tag{36}$$

$$e_2 = 4.809 \cdot 10^{-6} \cdot (2\alpha)^2 - 2.346 \cdot 10^{-3} \cdot (2\alpha) + 0.3400 \tag{37}$$

With geometries of blunt notches it is possible to link the parameter a_1 to the maximum principal stress at the notch tip by [8]:

$$a_1 = \frac{\sigma_{tip} r_0^{1-\lambda_1}}{1 + \tilde{\omega}_1} \tag{38}$$

Introducing the parameter H, with values depending on the opening angle and Poisson's ratio. Values of H are shown graphically in figure 6.13. The mean value of SED for blunt notches of mode 1 can be expressed as [28]:

$$\overline{W}_1 = \frac{H \left(2\alpha, \frac{R_0}{\rho} \right)}{E} \left[\frac{K_{R,1}^V}{R_{0s}^{1-\lambda_1}} \right]^2 \tag{39}$$

The radius of the volume for fatigue loads $R_0 f$, is calculated using Poisson's ratio as for static load, but instead of using σ_{UTS} and the K_{IC}, the use of $\Delta\sigma_a$ and K_{1C} are substituted into the equation 40 [23].

$$R_{0f} = \left(\frac{\Delta K_{IC}^N}{f_1(2\alpha)\Delta\sigma_A} \right)^{\frac{1}{(1-\lambda_1)}} \tag{40}$$

Where $f_1(2\alpha)$ is calculated by the simplified expression below for Poisson's ratio still equal to 0.3. With the same simplified estimations as for e_i given in equation 41 [23].

$$f_1(2\alpha) = 4.897 \cdot 10^{-5} \cdot (2\alpha)^2 - 5.598 \cdot 10^3 \cdot (2\alpha) + 1.959 \tag{41}$$

14

Substituting the NSIF to the NSIF-based fatigue strength ΔK_i in the relevant equation. Fatigue SED can be graphically displayed with a $\Delta \overline{W} - N$ curve with $\Delta \sigma_A$ at a given cycles to failure. SED offers a good failure approximation of brittle and quasi-brittle notched components with a graphical display of over 900 experimental data of various steels in figure 5.15.
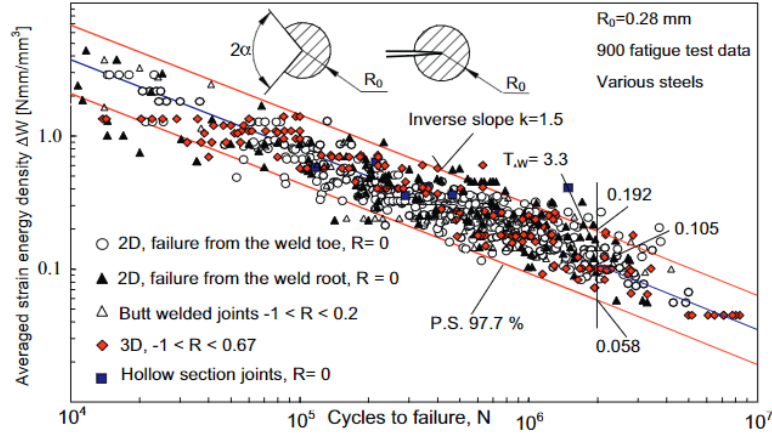

Figure 5.15: Example of ΔW-N curve. 900 experimental data including butt welded joints, three-dimensional models and hollow section joints performed by Berto et al. [8].

Mesh sensitivity for SED calculations in FEA was demonstrated by Lazzarin et al. [29] [9], with difference in results of SED between the finest and the coarsest mesh reported to be less than 5%. The FE analysis is not mesh sensitive because the elastic strain energy is directly determined by the nodal displacements. This is without calculations involving stress and strains, where derivatives of the displacements take place [30]. The total strain energy stored in the finite element is:

$$E_t = \int_V W dV = \frac{1}{2}\{d\}^t \left(\int_V [B]^t[E][B]dV \right) \{d\} = \frac{1}{2}\{d\}^t[K]\{d\} \qquad (42)$$

Where V is the volume and the stiffness matrix [K] of the finite element being:

$$[K] = \int_V [B]^t[E][B]dV \qquad (43)$$

The theoretical approach for the FE methods starts with the vectors of the displacement and the forces.

$\{d\}$: vector of nodal displacements.
$\{f\}$: vector of nodal forces.

It is possible to express the displacement vector $\{u\}$ and thereby also the strain vector $\{\epsilon\}$, by introducing the displacement interpolation matrix $[N]$. Which is dependent on the FE type.

$$\{u\} = [N]\{d\}, \quad \{\epsilon\} = \frac{\partial\{u\}}{\partial x_i} = [B]\{d\} \qquad (44)$$

15

[B] is the strain-displacement matrix, which is obtained by differentiating the rows of [N]. Stress and strain are linked together by linear elastic hypothesis $\{\sigma\} = [E]\{\epsilon\}$. Returning to equation 26, giving the strain energy density in a point, belonging to an finite element W:

$$W = \frac{1}{2}\{\epsilon\}^t\{\sigma\} = \frac{1}{2}\{d\}^t[B]^t[E][B]\{d\} \tag{45}$$

5.5.1 Equivalent Material Concept

Torabi proposed in 2012 his theory of Equivalent Material Concept (EMC) [31] where he equated a real ductile material with elastic-plastic behaviour with a virtual brittle material with perfect elastic behavior. Similar to that proposed by Glinka et al. [32], but with a different approach. He fitted the tensile stress-strain relationship in the plastic region of the ductile material by the power law and computed the total SED to the peak point, see figure 5.16.
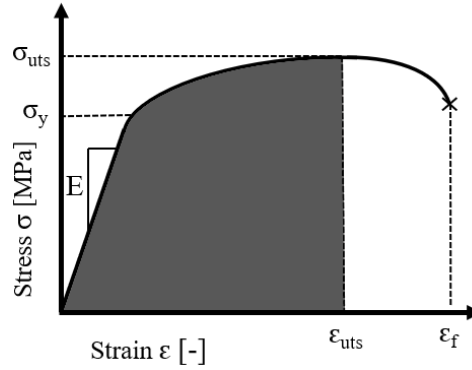
Figure 5.16: A typical stress-strain curve showing absorbed SED till necking

Then the assumption was made that the ductile and virtual elastic material absorbed the same amount of tensile SED until a brittle fracture occur. The total SED of the real ductile material was calculated by adding the elastic with the plastic SED until necking as shown in the equation below.

$$(SED)_{tot} = (SED)_{elastic} + (SED)_{plastic} = \frac{1}{2}\sigma_y\epsilon_y + \int_{\epsilon_p^y}^{\epsilon_p} \sigma d\epsilon_p \tag{46}$$

Combining the previous equation with the power law 6 into a single equation for total SED.

$$(SED)_{tot} = \frac{\sigma_y{}^2}{2E} + \int_{\epsilon_p^y}^{\epsilon_p} H\epsilon_p^n d\epsilon_p = \frac{\sigma_y{}^2}{2E} + \frac{H}{n+1}\left[(\epsilon_p)^{n+1} - (\epsilon_p^y)^{n+1}\right] \tag{47}$$

ϵ_p^y is the true plastic strain at yield point and is considered to be equal to the 0.2% offset (0.002) giving:

$$(SED)_{necking} = \frac{\sigma_y{}^2}{2E} + \frac{H}{n+1}\left[(\epsilon_{u,True})^{n+1} - (0.002)^{n+1}\right] \tag{48}$$

With both materials exhibiting the same Young's modulus and fracture toughness, the SED_{EMC} until fracture can be written as:

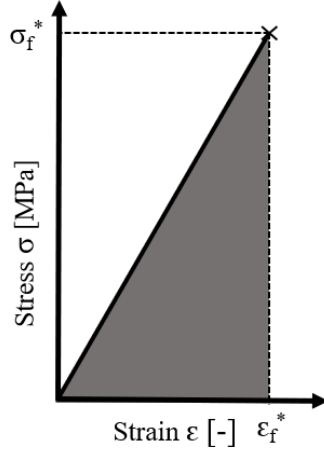$$(SED)_{EMC} = \frac{\sigma_f^{*2}}{2E} = (SED)_{necking} \tag{49}$$

Figure 5.17: A perfectly elastic stress-strain curve of an equivalent brittle material showing absorbed SED before failure

With eventually creating a closed-form equation of the EMC for calculating the fracture stress σ_f^*.

$$\sigma_f^* = \sqrt{\sigma_y + \frac{2EH}{n+1}\left[(\epsilon_{u,True})^{n+1} - (0.002)^{n+1}\right]} \tag{50}$$

With σ_f^* computed together with a valid fracture toughness can form the basis of different brittle failure criteria such as TCD and SED, predicting crack initiation in ductile materials weakened by stress risers.

Research made by Fuentes et al. [33] showed that EMC combined with SED or TCD made good failure predictions without any previous calibration of the model. But in members with larger notch radii the results where under-conservative for both methods. Still they are recommended because they are easy to perform with no time-consuming elasto-plastic analysis. EMC-SED discrepancy are shown in figure 5.18
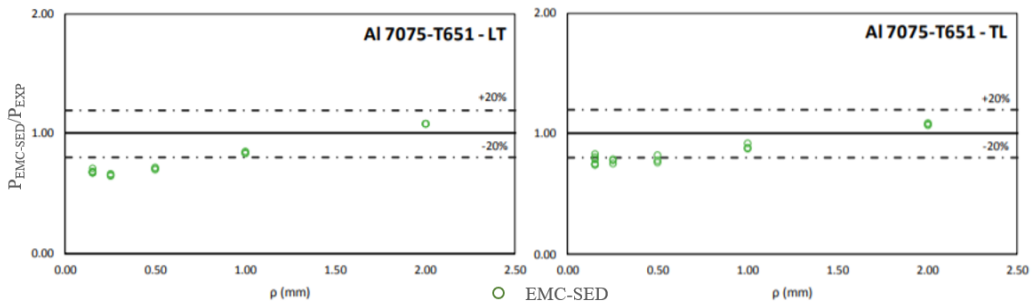
Figure 5.18: Fracture load prediction for longitudinal and transverse specimen by EMC combined with SED from [33]. Most results within $\pm20\%$, with conservative results for all but notch radius equal to 2*mm*.

5.5.2 Equivalent Strain Energy Density

Equivalent strain energy density (ESED) criterion was formulated by Glinka and Molski [32] and [34], and later re-formulated by Lazzarin et al. [35]. This theory states that the elasto-plastic strain energy density of a finite volume in the vicinity of the notch tip is coincident with that determined under pure elastic conditions. Through the use of plastic notch stress intensity factor makes it possible to quantify the intensity of the elasto-plastic stress and strain field in the vicinity of a sharp V-notch tip described in equation 51.

$$W^E(r,\theta) \propto r^{2(\lambda_1-1)}, \quad W^P(r,\theta) \propto r^{-s(n+1)}. \tag{51}$$

Where the elasto plastic singularity, s, is calculated using:

$$s = \frac{2(1-\lambda_1)}{(n+1)} \tag{52}$$

The local plastic SED is determined using both strain hardening parameters, stress singularity, as well as the elastic- and plastic integral of the stress field shown in equation 53. The angle γ is explained in figure 5.19.

$$\overline{W}_{local}^P(R) = \frac{n}{(n+1)H^n} \cdot \frac{I_p(\gamma,n)}{\gamma(2-s(n+1))} \cdot \left(\frac{K_{1p}^N}{R_0^s}\right)^{n+1} \tag{53}$$
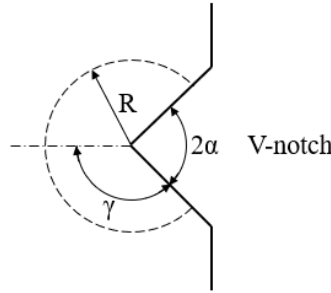
Figure 5.19: Angle γ in the coordinate system of a V-notch.

With the plastic integral of the angular stress functions in equation 54, where $\widetilde{\sigma}_e$ is the angular distribution of the equivalent stress for Mode I loading.

$$I_p(\gamma,n) = \int_{-\gamma}^{+\gamma} \widetilde{\sigma}_e(\theta)^{n+1} d\theta \tag{54}$$

Under the hypothesis that the amount of energy concentration, K_W, are equal under elastic and plastic conditions:

$$K_W^P(R) = K_W^E(R) \tag{55}$$

Gives equal energy concentration condition the plastic NSIF (P-NSIF) can be determined by an elastic FE-analysis, where the elastic NSIF is [36]:

$$K_1^N = k_1 t^{(1-\lambda_1)} \sigma_{nom} \tag{56}$$

Then the P-NSIF can be expressed as:

$$K_{1p}^N = \left[\frac{n+1}{n} \cdot H^n \cdot \frac{I_e(\gamma)}{I_p(\gamma)} \cdot (k_1 t^{(1-\lambda_1)})^2 \cdot \left(\frac{\sigma_{nom}^2}{2E} + \frac{n}{n+1} \cdot \frac{\sigma_{nom}^{n+1}}{H^n} \right) \right]^{\frac{1}{n+1}} \quad (57)$$

The P-NSIF can also be calculated through the use of the NSIF, the opening angle and material parameters, but only if localized yielding conditions are present in equation 58 and a comparison in figure 5.21.

$$K_{1p}^N = A \cdot (K_1^N)^b \quad (58)$$

$$A = \left(\frac{n+1}{n} \cdot \frac{H^n}{2E} \cdot \frac{I_e(\gamma)}{I_p(\gamma)} \right)^{\frac{1}{n+1}}, \quad b = \left(\frac{2}{n+1} \right). \quad (59)$$

Lazzarin et al. reported an accurate correlation between equation 57 and 58 with FEM below large scale plasticity. Equation 57 has no upper limit for applicability both for tensile and bending condition, while 58 show a reasonably high accuracy for both low and large scale plasticity with bending. The analytical- and numerically obtained stressfields are shown in figure 5.20.
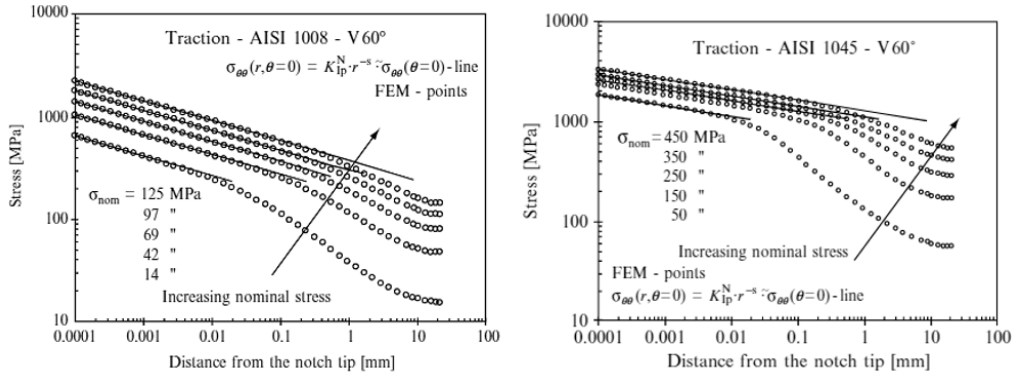
Figure 5.20: Plots of σ_θ along the notch bisector. AISI 1008; $1/n = 4$, $H = 600MPa$ and $\sigma_y = 125MPa$. AISI 1045, $1/n = 8.33$ and $H = 950MPa$ and $\sigma_y = 450MPa$ [35].
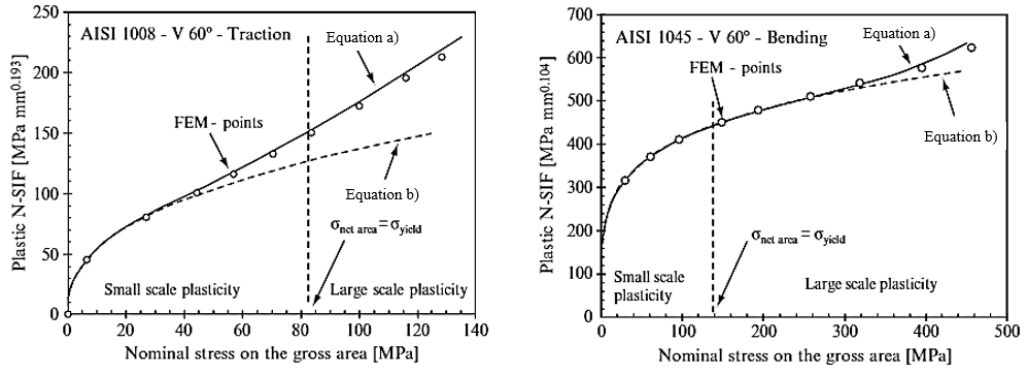
Figure 5.21: Difference of accuracy between traction and bending for two different steels [35]. a) Equation 57, and b) equation 58.

19

5.6 Additive Manufacturing

Additive manufacturing (AM), according to ASTM (2012). "Can be defined as a collection of technologies able to join materials to make objects from 3D model data, usually layer upon layer, as opposed to subtractive manufacturing methodologies". Charles Hull was the first to receive a patent for a machine creating 3D objects using stereolitograph [37]. Modelling components by AM was first a popular choice for rapid prototyping, but in recent days it has become a possible production method for components too [38]. The three main branches of AM productions methods are shown in figure 5.22. Powder material production is most common when making components of metal, but is also used for polymers.
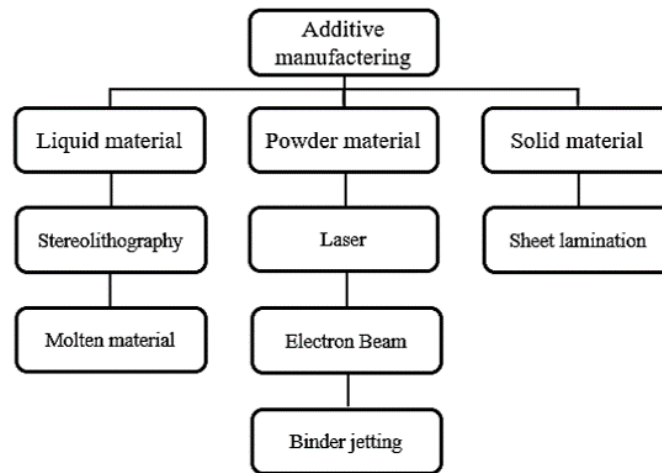
Figure 5.22: Branches of AM [39].

AM is usually performed by an layer-upon-layer manner, where a digital model is required in a computer assisted design (CAD) program, either drawn or made from scanning a pre-made component. The file is later converted to a STL fil format, where the 3D model is «sliced» into layers. Lindemann et al. [7] reported in 2012 the main advantages and disadvantages of AM listed below.

Advantages:

- More flexible development.

- Freedom of design and construction.

- Less assembly.

- No production tools necessary.

- Less spare parts in stock

- Less complexity in business because of less parts to manage.

- Less time-to-market for products.

- Faster deployment of changes

Disadvantages:

- High machine and material costs.

- Quality of parts is in need of improvement.

- Rework is often necessary (support structures).

- Building time depends on the height of the part in the building chamber

Production costs of AM are almost independent of component complexity and by production number, contrary to ordinary manufacturing where high costs are associated with complex geometry and low production numbers [38]. The component can be made anywhere there is an appropriate AM production facility. However, larger cost of machine and materials, together with lower quality of parts prohibits companies of investing in this technology. Many researches are therefore focused on improving it.

5.6.1 Selective laser melting

SLM uses a high-energy laser beam in which to fuse together powder materials in a selective manner. It was first developed by Dr. M. Fockele and Dr. D. Schwarze of F S Stereolithographietechnik GmbH, with Dr. W. Meiners, Dr. K. Wissenbach, and Dr. G. Andres of Fraunhofer ILT and introduced to the marked in 1998 [40]. It was invented for the purpose of making components of metal. The process consist of a powder bed on a moving platform within an inert gas atmospheric chamber. The components are built on the moving platform where the laser first melts a thin layer of powder material to the substrate platform. Metal powders are usually of the size 20-100 μm [40] seen in figure 5.23.
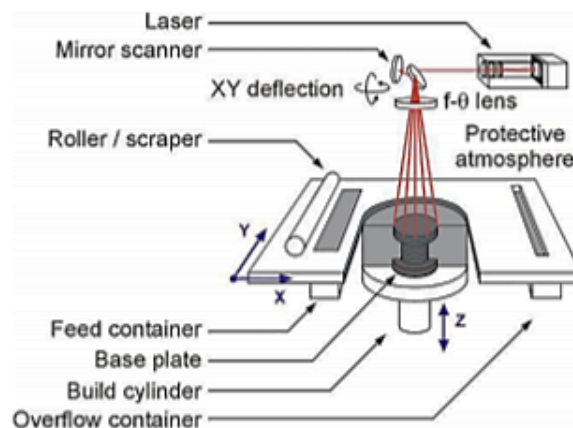
Figure 5.23: Schematic view of a SLM machine [41].

This platform moves in the z-direction after a layer has been made, where a new layer of powder is evenly distributed by a coating mechanism. A new layer is selectively melted according to the STL model, partly melting and fusing it to the previous layer, repeating until a complete model is made. The model is then removed from the substrate platform and later separated from the build supports. Producing components by laser involves parameters such as; laser power,

scanning speed, hatch spacing, and layer thickness are the common process parameters adjusted to optimize the process seen in figure 5.24.
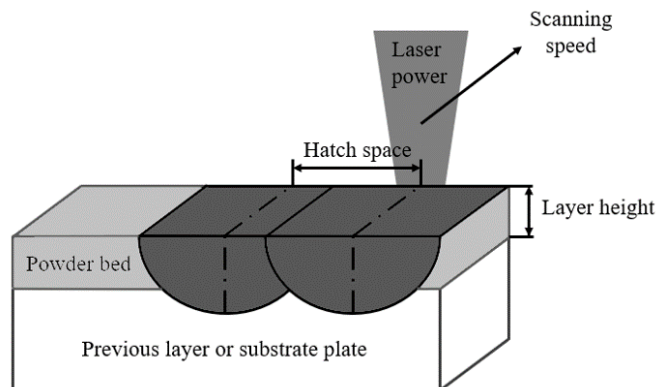

Figure 5.24: Powder bed additive manufacturing settings by laser scanning.

An example of a complex component geometry is shown in figure 5.25, which my roommate mistakenly thought was the traditional Norwegian Christmas food "pinnekjøtt".
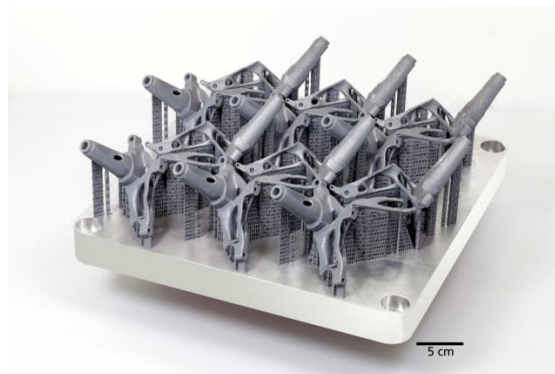

Figure 5.25: AM offers great geometry complexity. This figure shows twelve wheel bearings on a base plate with build supports underneath made by SLM. (Image courtesy of Fraunhofer EMI.)

The component properties by SLM give a rougher surface finish than most conventional methods, and inherent flaws such as porosity and surface defects of inclining surfaces are still a concern, where some geometries needs build support that must be removed afterwards. AM components also contain residual stresses and distortions due to the complex thermal and phase transformation stresses during the localized heating [41]. The expansion and contraction of the previously solidified layers happens frequently and can cause devastating thermal stress and stress gradients surpassing the yield strength. Residual stress can be minimized by means of heat treatments [39]. Surface roughness can be handled by shoot-peening, and porosity can be minimized by means of hot isostatic pressing. Materials such as Ti-6Al-4V, 316L stainless steel together with IN 718 have all been reported to achieve more than 99.9% relative density in Yap et al. [40] by SLM.

5.6.2 Hot Isostatic Pressing

Hot isostatic pressing (HIP) is a common means to treat post-manufacturing, with main focus to remove pores within the component [42]. It is already in use on castings, to densify presintered components, solidification of powders and interfacial bonding of similar or different materials. HIP is a procedure where the component is exposed to both heat and pressure. The process consists of a pressurized and heated chamber with an inert gas seen in figure 5.26. Here the component is subjected to an uniform pressure and a temperature approximately 70% of the melt temperature (TM).
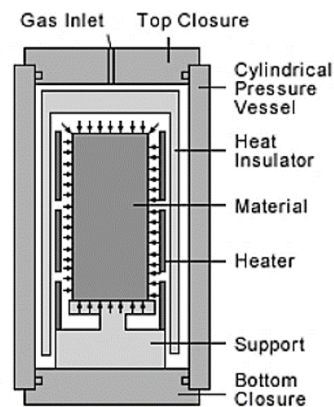
Figure 5.26: Example of HIP chamber [43].

By combining heat and pressure creates a lower temperature needed than in sintering [44], and a lower pressure than chipping. This avoids unwanted grain growth and eliminate the need of additives to enhance densification. HIP compresses the material without changing the size and shape, densifing it by dissolving pores into the matrix down to pore sizes of approximately $40nm$. Figure 5.27 show properties enhanced by HIP such as internal porosity in as cast components, creating comparable properties as forged components. HIP can also be beneficial in reducing property scatter. It is because of high costs, associated with more exotic material which is difficult to fabricate or treat by other means [44].
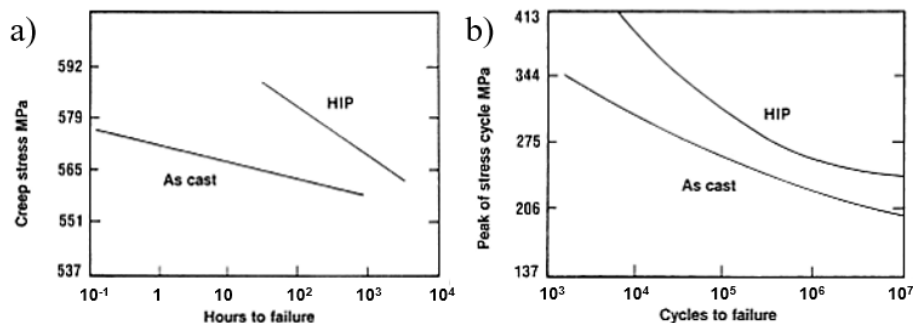
Figure 5.27: Fatigue strength and creep resistance enhanced by HIP on as cast members [44]. a) Creep life of Ti-6Al-4V at 399^oC. b) Fatigue life of Ti-6Al-4V at 316^oC.

23

5.7 Nickel based super alloys

In nickel based alloys a two phase equilibrium is generated when introducing a concentration of Al and or Ti up to 10% by weight [4]. It consist of the states, gamma (γ) and gamma prime (γ'), in which γ' is mostly responsible of determining the inherent elevated temperature strength and great creep resistance. The alloy can be further strengthened at lower temperature by another phase called gamma double prime (γ'') with chemical composition of Ni3(Nb,V). The ternary phase diagram for given chemical compositions show a fraction decrease of γ' when the temperature is increased seen in figure 5.28.
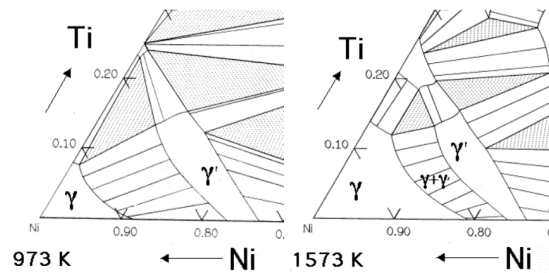
Figure 5.28: The ternary phase diagram for nickel based superalloys [4]

The solid solution phase of γ, has a face-centred cubic structure (FCC). The atoms of the material compound is randomly distributed in the lattice structure. γ', has a primitive-centred cubic lattice (PCC) with a similar lattice parameter to that of FCC. It differ from FCC by a set arrangement of nickel in the face centers, and with Al or Ti in each corners of the cube. This has a chemical formula of Ni3(Al, Ti). But because the phase is not strictly stochiometric, there may be an excess of vacancies in which nickel atoms might rearrange with aluminum. γ'', has a body-centred tetragonal lattice (BCTL). This lattice is also of ordered arrangement. It consist of Nb in each corner and of Ni elsewhere, see figure 5.29.
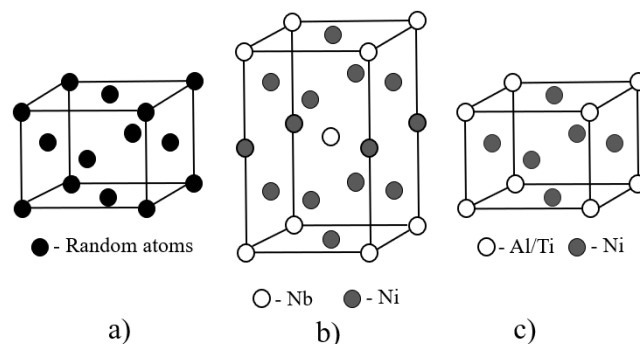
Figure 5.29: a) Face-centred cubical γ-structure. b) Body centred tetragonal lattice - γ''. c) primitive-centred cubical γ'-structure

γ' precipitates from the γ-matrix. The precipitation of γ' in relationship with γ occurs in a cube-cube orientation because of their similar lattice parameter, creating perfectly aligned cell edges. γ' is coherent with γ when the precipitate size is sufficiently small, but dislocations struggle to penetrate γ' because of its

atomically ordered phase. This causes a strengthening affect of the nickel superalloy. Most metals exhibit a decrease in strength at elevated temperatures. This is because thermal activation makes it easier for dislocations to pass obstacles. Ordinary slip in nickel based super alloys containing γ and γ' occurs on the 111<110> plane, causing a normal decrease in strength at elevated temperature. However, dislocations in γ' tend to cross-slip on to the 100 plane with a lower anti-phase domain boundary energy because the energy decreases with higher temperature. This locks the dislocations because it is partly on the close-packed plane and the cube plane, increasing the strength. Thermal activation is only sufficiently strong when exceeding about 600^oC. Higher strength at lower temperature can be achieved by a coherency and ordered hardening of γ'' seen in figure 5.30 a) because of sufficient amounts of niobium or vadium.
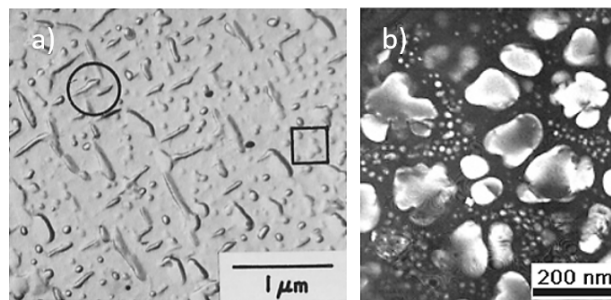
Figure 5.30: a) Circle showing γ'' and square showing γ' [45]. b) Fine dispersion of bimodal γ'. (Image courtesy of R. J. Mitchell) [4].

The microstructure in nickel based super alloys are heavily influenced by the heat treatment and are often given a solution treatment that determines the amount of dissolved γ' and also the grain size of γ. There is no pinning effect of the movement of γ'/γ boundaries if the precipitate particles of the γ' are all dissolved, thereby making the grains courser. Later they are treated at two different temperatures. The first treatment at high temperature is to precipitate coarser particles of γ', while the next treatment at a lower temperature is to further precipitate into a finer secondary dispersion of γ' as shown in figure 5.30 b). Some less desirable precipitates are called leaves or δ-phase (Ni_3Nb). This is more thermodynamically stable and under high thermal exposure is converted from γ''. It has a needle or plate like morphology in figure 5.31 a). Figure 5.31 b) show an example of a carbide.
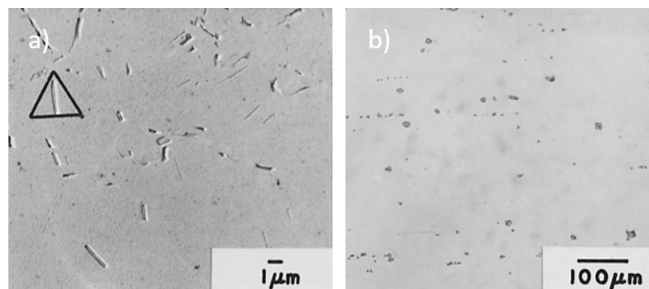

Figure 5.31: Leaves and carbides in IN718 [45]. a) Triangle showing a needle shaped leaves precipitate δ. b) Carbides of TiN and NiC.

5.7.1 Inconel 718

IN718 is a nickel-based superalloy which exhibits excellent mechanical properties at high temperatures, even in excess of 70 % of the melting temperature [4]. It has a high resistance to creep, great resistance to oxidation, and as one of the fist superalloys, also showed good weldability. It is a popular choice in aerospace industry and in other appliances where extreme conditions occur. Table 1 show some material parameters of IN 718

Material property	Unit	Value	Reference
Density	$[g/cm^3]$	8.19-8.22*	[46] [47]
Melting point	$[C^o]$	1260-1336	[46][3]
Thermal Conductivity	$[W/m \cdot k]$	6.5**-11.4	[46] [47]
Specific heat	$[J/kg \cdot K]$	435	[47][3]
Coefficient of thermal expansion	$[\mu m/m \cdot K]$	13.0-13.9	[47]
Electrical resistivity ($20C^o$)	$[n\Omega \cdot m]$	1210-1270*	[46] [47]

Table 1: General material properties for IN 718. * From annealed to aged condition. ** Between $(0 - 100C^o)$.

5.7.2 Material behavior of conventional IN718

Conventional IN 718 is covered by many standards for production method and heat treatment. Some of these are: AMS 5596B, AMS 5662, AMS 5663, AMS 5664, AMS 5832, AMS 5962, ASME SB-637, ASTM B637, AWS A5.14 and NACE MR0175 (ISO 15156-3). A general material composition is listed in table 9.

Weight %	Min	Max
Al	0.20	0.80
B		0.006
C	0.02	0.08
Co		1.00
Cr	17.00	21.00
Cu		0.3
Fe *	15.00	21.00
Mn		0.35
Mo	2.80	3.30
Nb+Ta	4.75	5.50
Ni	50.00	55.00
P		0.015
S		0.015
Si		0.35
Ti	0.65	1.15

Table 2: Chemical composition in accordance with AMS specifications [3]. * Or balance.

Conventionally wrought material need δ precipitates to pin the grain boundaries during forging to achieve fine grains. Some material properties to expect from IN718 is shown in the following table 3 with values from [3]. (The specimens

tested was hot-rolled flat heat-treated at 982°C for 1 hr, A.C at 718°C for 8 hour, F.C. -7°C for hr to 621°C, held for total aging time of 18 hr.)

Material property	Symbol	Unit	-66C^o	21C^o	649C^o	982C^o
Young's modulus	E	[GPa]	211*	200	163	120
Torsional modulus	G	[GPa]	81*	77	63	45
Ultimate tensile strength**	σ_{uts}	[MPa]	-	1241	965	-
Yield strength**	σ_y	[MPa]	-	1034	862	-
Poisson's ratio***	ν	[-]	0.30	0.294	0.283	0.341

Table 3: Mechanical properties of In 718 at different temperatures. $*$ Cold-rolled sheet heat-treated in accordance with AMS 5596B. $**$927-1010C^o anneal with its corresponding aging treatment and tested according to AMS 5662 transverse for bars. $* * *$ Calculated from $(E - 2G)/2G$. Values from [3].

Suggested operating temperatures are from -200^oC up to 650^oC [48]. IN718 is little affected by temperature to about 650C^o, where the thermally activated dislocations eventually dislocate through the lattice. A disadvantage for the material is otherwise its advantage, the high strength, toughness and ability to work harden [49]. This makes ordinary manufacturing methods difficult and expensive. The workpiece can be heated to exceed approximately 540 C^o to be machined for better convenience.
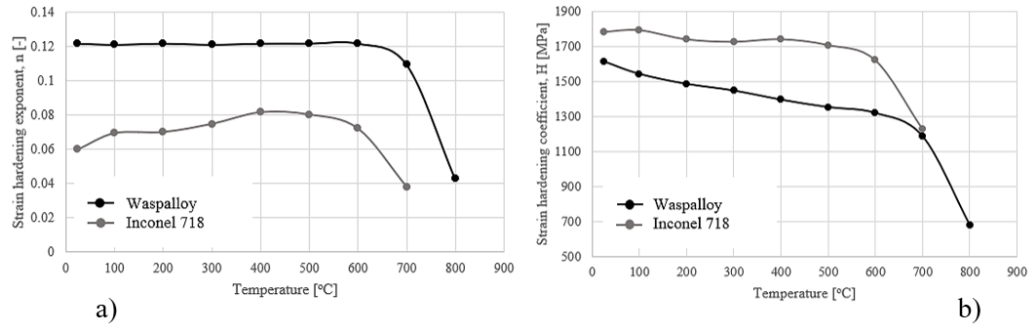
Figure 5.32: Ramberg-Osgood parameters of IN718 compared to Waspalloy at different temperatures [50]. a) Strain hardening exponent. b) Strain hardening coefficient.

Vickers hardness to expect ranges from 230 to 410 ($HV_{1.0}$), with other material properties compared from the test given in table 4, where strain hardening parameters are also included. The strain hardening parameters differ slightly from figure 5.32, with lower H and higher n. The aged IN 718 from table 4 looses ductility while gaining strength compared with annealed state.

Treatment	σ_y	σ_{uts}	Elong. [%]	Hard. ($HV_{1.0}$)	n	H [MPa]	Ref.
Annealed	430	843	51.4 ± 0.7	236.4 ± 5.2	0.264	1467.8	[51]
Aged	823	1090	41.2 ± 3.9	408.5 ± 3.2	0.119	1482.0	

Table 4: Hardness and strain hardening parameters for CM.

Fracture toughness has been reported to be between 120.5-171.4 $MPa\sqrt{m}$ based on the post production treatment [52]. However values obtained in the same report suggested possible fracture toughness of 62.5 $MPa\sqrt{m}$ of conventionally treated, though requirements of ASTM E399-74 where not fully met. Heat treatments are explained in [52]. The same test suggested a fracture toughness at 427 ^oC of 57.7 $MPa\sqrt{m}$. Liu et al. [53] tested the anisotropy of the fracture toughness in aged IN 718 shown in figure 5.33 where also the material direction of the tests are shown.
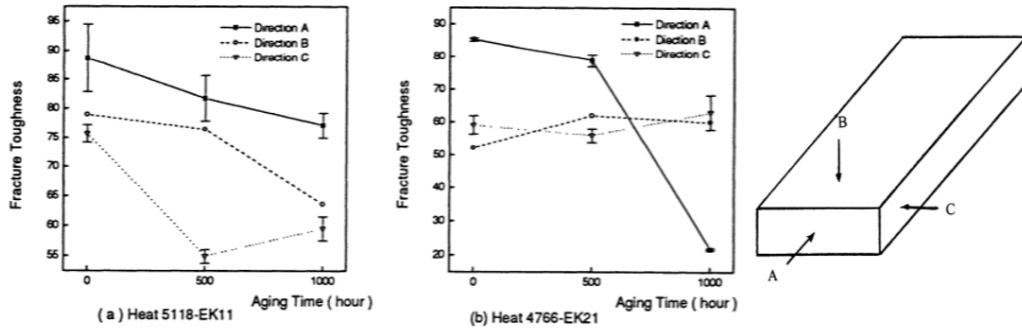
Figure 5.33: Anisotropy of fracture toughness with different aging time [53].

Both heats were given a conventional heat treatment consisting of a solution anneal at 950 ± 14^oC for 1 hour, air cooling to room temperature, aging at 718 ± 8^oC for 8 hours, furnace cooling to 621^oC, and aging at 621 ± 8^oC, to give a total precipitation time of 18 hours. Heat treated pieces from each of the two heats were exposed to 649^oC for times of 0, 500, and 1000 hours.

Fatigue of IN 718 with values from the literature are shown in table 5. Zhong et al. [54] created a quadratic function with good agreement of the relationship between σ_{uts} and σ_{-1} from the values in table 5, being: $\sigma_{-1} = \sigma_{uts} \cdot (0.869 - 3.67 \cdot 10^{-4} \cdot \sigma_{uts})$.

Load type	Stress ratio	σ_{uts}	σ_{-1}	Ref.
Axial	-1	940	492	[54]
Axial	-1	1560	461	
Axial	-1	1549	420	[55]
Axial	-1	1458	440	[56]
Rotating bending	-1	1390	500	[57]
Rotating bending	-1	1460	460	[58]
Axial	0.01	1369	380	[59]
Axial	0.1	1343	450	[60]

Table 5: Fatigue properties ($N_f = 10^7$) of IN 718 versus ultimate tensile strength. Note: approximate fatigue properties obtained from [54], but referring to their original paper. Fatigue strength approximately 34% of σ_{uts}.

Results obtained by Kawagoishi et al. [58] in figure 5.34 of fatigue performance at different temperatures, shows an increase in fatigue strength up to 500^oC. The strength decreased from 500^oC to 600^oC, but was still higher than for RT.
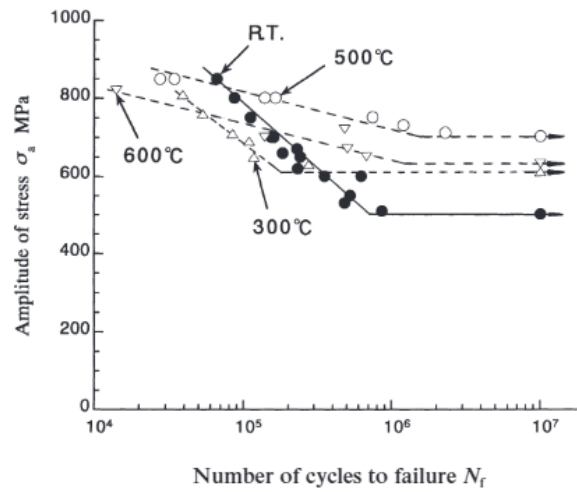
Figure 5.34: Endurance curves for plane specimen at stress ratio, R=-1 [58].

Crack growth rate obtained from NASA [61] seen in figure 5.35 show a crack threshold value of approximately $\Delta K_{th} = 10 MPa\sqrt{m}$.
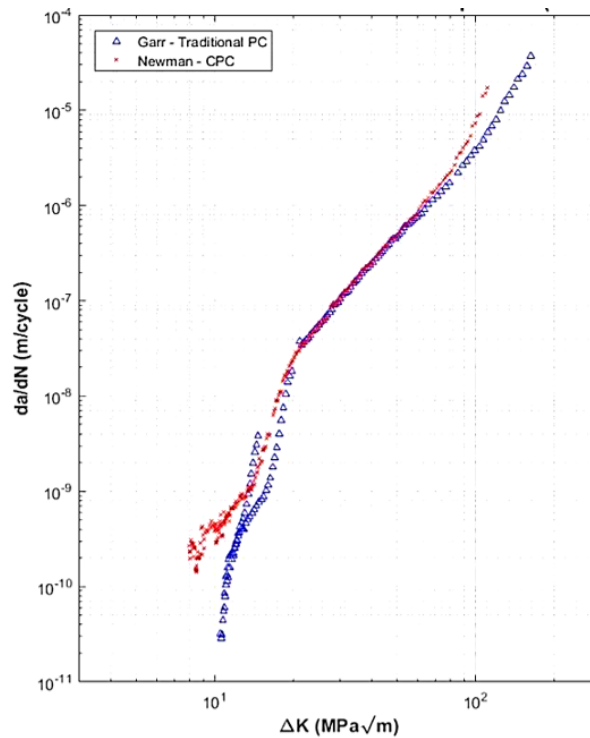
Figure 5.35: Crack propagation data at load ratio $R = 0.1$ [61]

The study of Xiao et al. [62] showed an increase in the fatigue crack propagation threshold, ΔK_{th}, which in this study was defined as the ΔK corresponding to a growth rate of $10^{-10} m/cycle$. It increased from 7.6 to $8.6 MPa\sqrt{m}$ at room temperature as the boron concentration increased from $12ppm$ to $29ppm$.

5.7.3 Material behavior of AM IN718

The material composition used for AM by industry is similar to the chemistry of conventional compound, but have a lower acceptance of Si content of 0.15% [63]. The standard ASTM F3055 - 14a covers the specification for additive manufacturing nickel alloy (UNS N07718) with powder bed fusion.

*	Min	Max
Al	0.40	0.70
B		0.006
Bi,ppm		0.3
Ca		0.01
C	0.02	0.08
Co		1.00
Cr	17.00	21.00
Cu		0.3
Fe	15.00	21.00
Mg		0.01
Mn		0.35
Mo	2.80	3.30
N		0.020
Nb	4.75	5.50
Nb+Ta	4.75	5.50
Ni	50.00	55.00
O		0.020
P		0.02
Pb, ppm		5.00
S		0.015
Se,ppm		3
Si		0.15
Ta		0.05
Ti	0.85	1.15

Table 6: Powder lot composition [63]. * All values in weight percent unless otherwise specified.

A strong variability of material properties of IN 718 produced by AM is reported in the literature. Its inherent strength, stiffness and hardness depends on the production method, orientation of printing and printing properties such as laser speed and power. Table 7 show a large number of static material properties obtained by multiple authors at RT.

Type	*	Ori.	E	σ_y	σ_{uts}	Elong.	Hard.	Ref.
SMD	AP	XY	NA	473±6	828±8	28±2	NA	[64]
DLD	AP HT	Z	NA	650 1257	1000 1436	NA	NA	[65]
Laser	AP HT	NA	NA	590 1133	845 1240	11 9	NA	[66]
EBF	AP	XY	159	580	910	22	NA	[67]
EBF	AP HT	XY YX XY YX	138 194 174 192	655 699 986 998	978 936 1114 1162	NA	NA	[68]
DLD	HT	NA	NA	1098	1321	9.8	NA	[69]
DLD	HT	NA	NA	1034	1276	12	NA	[70]
Laser /wire	HT	NA	NA	1079	1314	20.4	NA	[71]
SLM 250W	AP HT	NA	NA	NA	NA	NA	303 446	[]
SLM 250W	AP HT	NA	NA	NA	NA	NA	290 415	[]
SLM 250W	AP HT HIP HT+HIP	NA	173±13 190±11 188±8 190±6	668±16 875±11 645±6 1145±16	1011±27 1153±4 1025±14 1376±14	22±2 17±2 38±1 19±1	320** 360** 310** 468**	[72]
SLM 950W	AP HT HIP HT+HIP	NA	113±3 138±5 183±19 188±20	531±9 668±7 481±11 1065±20	866±33 884±80 788±12 1272±12	21±5 7±2 34±3 15±4	287** 338** 262** 451**	[72]

Table 7: Static material properties at RT of AM IN718. * As produced or heat treatment.** HV_{1kgf}. Specimen orientation according to figure 5.36.

Effect of temperature on mechanical properties of SLM IN718 as produced or with post production treatment has been tested with values listed in table 8.

Type	Treatment	Temp.	σ_y [MPa]	σ_{uts} [MPa]	Elong. [%]	Ref.
SLM (275W)	AP HT	20^oC	569-646 1160	851-1002 1350	9.8-31.7 17.6	[73]
SLM (250W)	AP HIP HT+HIP	650^oC	650±11 626±8 942±11	845±9 857±14 1078±8	28±4 29±1 20±2	[72]
SLM (950W)	AP HIP HT+HIP	650^oC	543±2 479±5 872±13	782±6 665±7 1005±12	31±6 28±2 17±4	[72]
SLM (275W)	AP HT	1000^oC	112 113	114 116	47.5-53.5 58.1	[73]

Table 8: Mechanical properties of SLM IN718 at different temperatures, before and after heat treatment.

It is evident that heat treatment of AM specimen have a strong beneficial effect on both yield strength and ultimate tensile strength which can increase significantly. HT does also have a significant effect on material hardness with around 45% increase. However, the HT give in general a less ductile material.
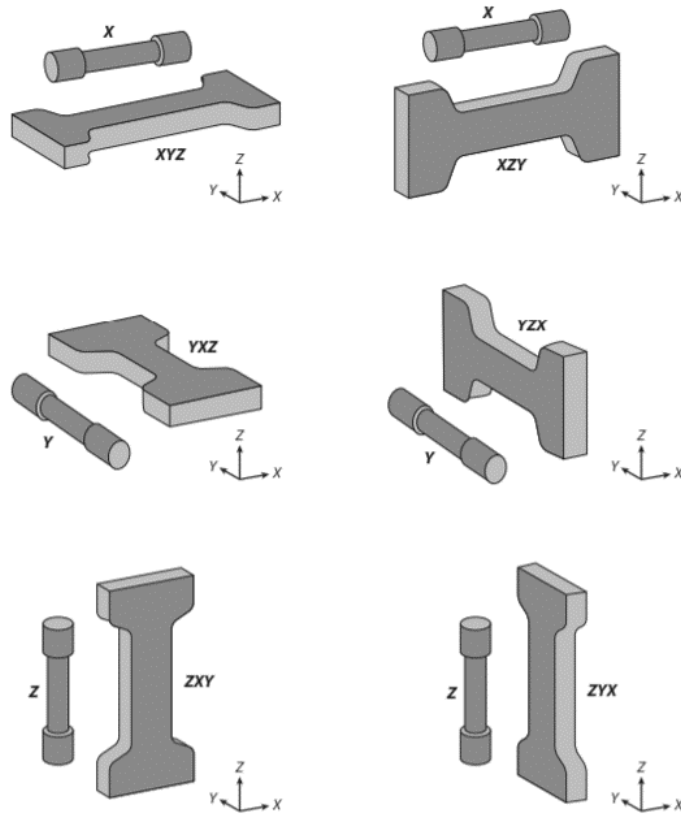
Figure 5.36: Specimen orientation according to table 7.

IN718 made by SLM have superior creep strength in comparison to conventionally wrought. This is due to the higher volume fraction of the strengthening phases combined with the process induced subgrains.

Data on fracture toughness collected by NASA [74], ranged from approximately 127.7-149.5 $MPa\sqrt{m}$ with stress relief: 1065°C for 1.5 hours; furnace cool, HIP: 1165°C, 100 MPa, 3-4 hours, AMS 5664 Solution Treat: 1066°C for 1 hour; air cool and AMS 5664 Age: 760°C for 10 hours; furnace cool to 650°C; treat for total of 20 hours. Values converted from J_{IC} toughness, with $K_{IC} = \sqrt{J_{IC}E}$.

Fatigue of AM IN718 have been the focus of many studies in recent years. However because the production methods are still progressing, the fatigue properties will continue to improve. Some studies of fatigue regarding directional- and notch dependence are included below.
Konečná et al. [75] studied the anisotropic directional fatigue strength of SLM members in plane bending with three different build orientations. The specimen where heat treated and notch surface was as produced. Specimen orientation

and microstructural anisotropy is shown in figure 5.37. $\sigma_{uts} = 1406$ MPa, yield stress $\sigma_{y0.2} = 1213$ MPa, elongation to rupture A=19 %.
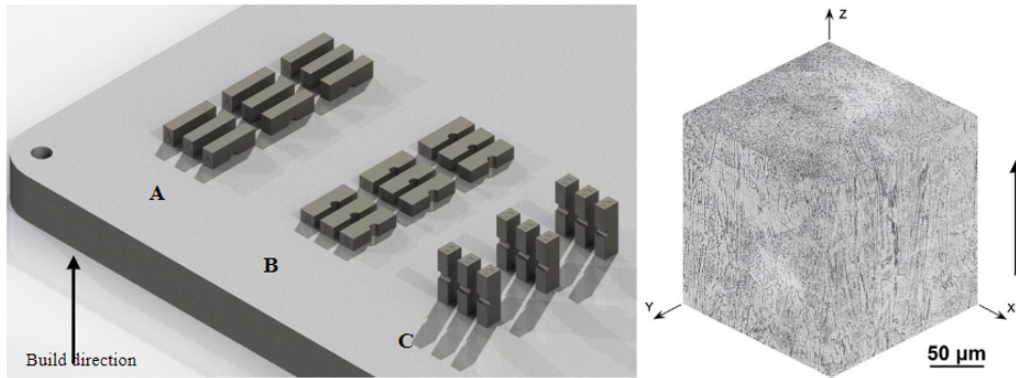
Figure 5.37: Different build orientations in left figure. Right showing microstructural anisotropy [75].
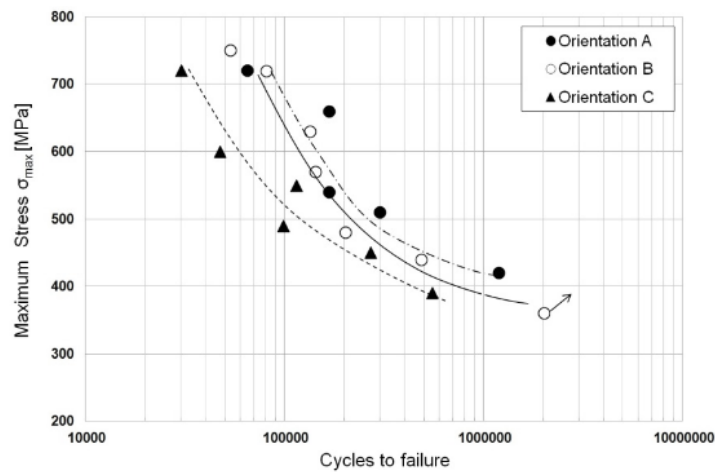
Figure 5.38: Directional fatigue properties with orientation according to figure 5.37, R=0, P=200W. Cycles to failure in log-scale [75].

Specimen type D showed less fatigue strength than the two others. Witkin et al. [63] reported in this study the fatigue notch effect of IN718 with three different notch geometries built in two direction seen in 5.39.
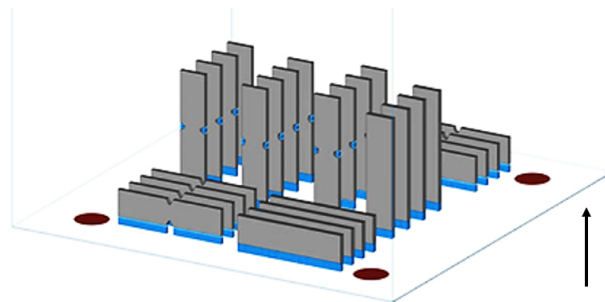
Figure 5.39: Build orientations with arrow indicating build direction. [63].

33

Both of AP AM specimen and AM specimen with machined notch, compared with conventional wrought specimen made from sheet metal. Results obtained from the fatigue test showed a build orientation dependence on the fatigue strength of the notch designs. The fatigue results are shown in figure 5.40.
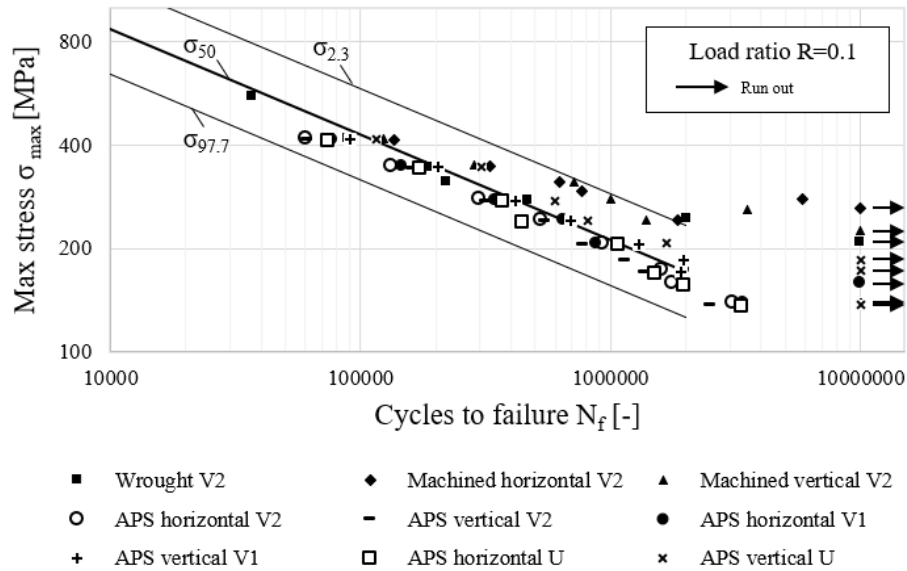
Figure 5.40: Fatigue results of IN718 specimen in log-log. Specimens were tested at the stress ratio R=0.1 and frequency of f=40Hz, according to the ASTM standard E466.
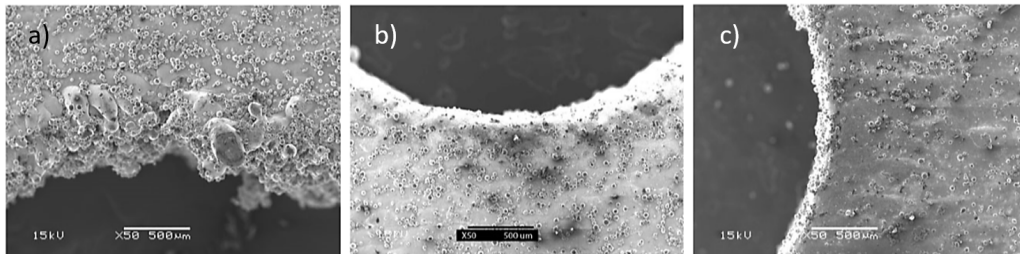
Figure 5.41: Different build orientation effect on U-notch surface [63]. a) Lower notch surface. b) Upper notch surface. c) Vertical notch.

V2 specimen had crack initiation at lower notch of the horizontally oriented V2 notch specimen. The figures in 5.41 show the notch surface roughness of different build orientations of the U-notch design. Figure 5.41 a) deviates from the others with a very rough notch root, that may have been created by residual stresses. The two other figures 5.41 b) and 5.41 c) show a much finer surface. The vertically built U-notch have the smoothest surface finish of these.

Solberg et al. [76] studied the fatigue notch sensitivity. The unnotched specimen had a fatigue strength at $N_f = 2 \cdot 10^6$ cycles, of 26% of the ultimate tensile strength, while the V-notched specimen with radius of 1mm decreased the strength down to only 12.6%. Results shown in figure 5.42.

34
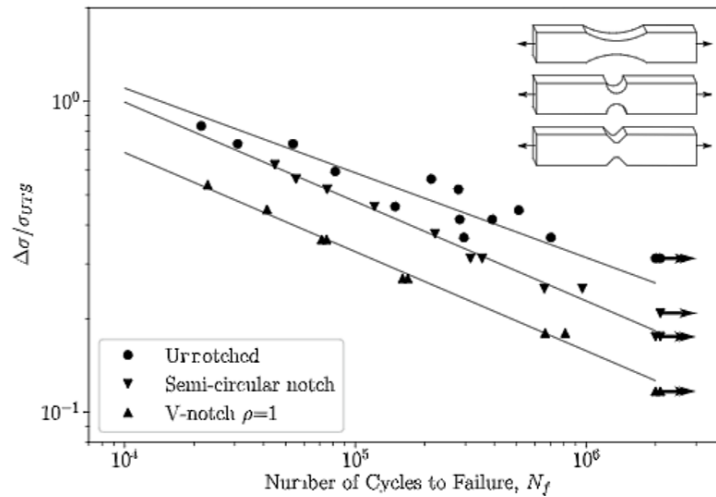
Figure 5.42: Fatigue results of IN718 specimen in log-log scale [76]. Where the V-notch of radius 1.0 mm being the same specimen as tested in this thesis.

Konečná et al. [77] found that crack growth in SLM specimen have a lower threshold than conventional ones, as seen figure 5.43. The crack growth's linear dependence in a log-log plot well approximates the crack growth rate data in the interval $1 \cdot 10^{-6}$ to $1 \cdot 10^{-4} mm/cycle$, according to the Paris equation values $da/dN = 2.25 \cdot 10^{-7} K_a^{2.31}$.
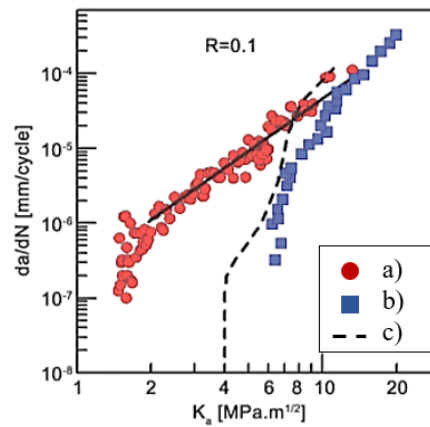
Figure 5.43: Crack growth in SLM versus conventional manufacturing. a) SLM [77], b) Conventional wrought [78], c) Conventional wrought IN 718 [79].

This comparison showed a significantly lower crack resistance of the SLM specimen, which had a crack initiation threshold of $K_{th} = 1.5 MPa\sqrt{m}$. However, the two different production methods gave a similar crack growth above $10 MPa\sqrt{m}$. These data are comparable because both specimen material compound had similar boron content, which is known to heavily influence the threshold crack growth value. A boron content between $12 ppm$ to $100 ppm$ is known to decrease the crack propagation rate [62].

35

6 Method

6.1 Test specimens

Test specimens was produced by standard processing parameters of SLM (LM) in Germany by Fit AG. They where produced layer by layer in the build direction indicated by the arrow in figure (6.1) where the dimensions of the specimen is showed. The layer height was $50\mu m$ with an energy density of $60J/mm^3$. No treatment was performed after the production was complete (AP).
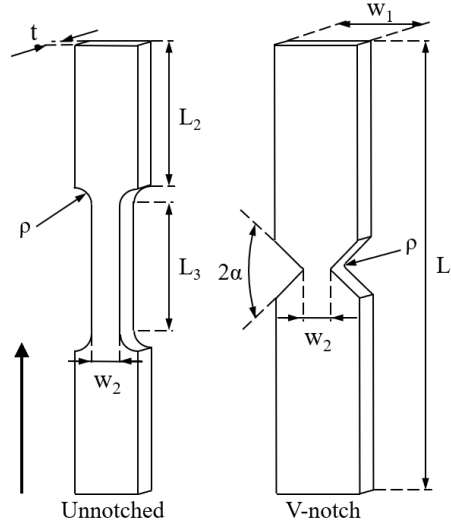
Figure 6.1: Specimen design dimensions with left arrow indicating build direction.

			Unnotched	V-notch
Height	L_1	[mm]	100	80
Length 2	L_2	[mm]	30	-
Length 3	L_3	[mm]	31.056	-
Width	W_1	[mm]	10	15
Nominal width	W_2	[mm]	6.0	5.82
Thickness	t	[mm]	3.0	5.0
Radius	ρ	[mm]	6.0	1.0
Opening angle	2α	[^{o}]	-	90
Notch sensitivity factor	K^*_{tnet}	-	1	2.43
Notch sensitivity factor	K^*_{tgross}	-	1	6.26

Table 9: Specimen dimensions. $*$ Obtained from FE-analysis.

6.2 Tensile test

A static tensile test was performed in order to investigate the failure assessment of the mean strain energy density criterion. In total three test was made, with two unnotched samples and one v-notch. The stress-strain tensile test of two unnotched specimen was performed with strain gauges to determine the Young's

modulus an accurate reading of the on plane specimen. Tensile tests where performed by the MTS Landmark servohydraulic test system with test data listed in table 10.

Specimen	Nr	Test speed [mm/min]	Failure force [kN]	Failure elongation [mm]	SG -
Unnotched	1	0.2	17.05	9.3	yes
Unnotched	2	0.8	16.86	9.2	yes
V-notched	3	0.8	34.02	1.6	no

Table 10: Tensile test data obtained.
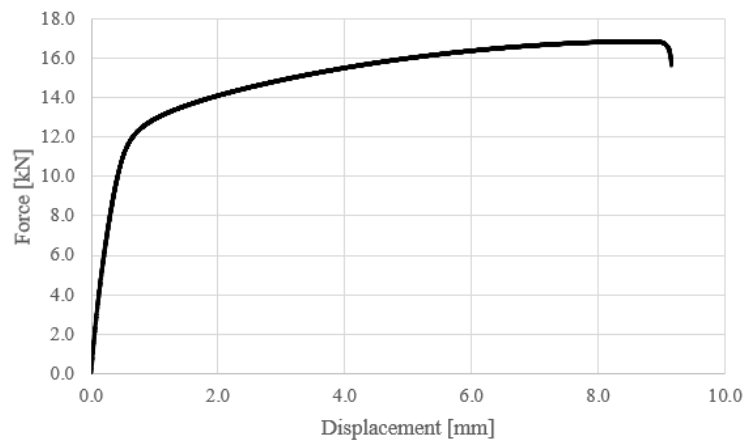
Figure 6.2: Static force versus displacement curve for unnotched specimen.

Test nr 1 and 2 had strain gauge (SG) failure during their tests. But the data collected from the SG was still used to determine the Young's modulus because the failure was evident on the data collected long after yielding. A combination of data from SG and the force versus displacement curve was used to create a stress-strain curve for the plane unnotched specimen. This was to be able to obtain Ramberg-Osgood parameters for the material.
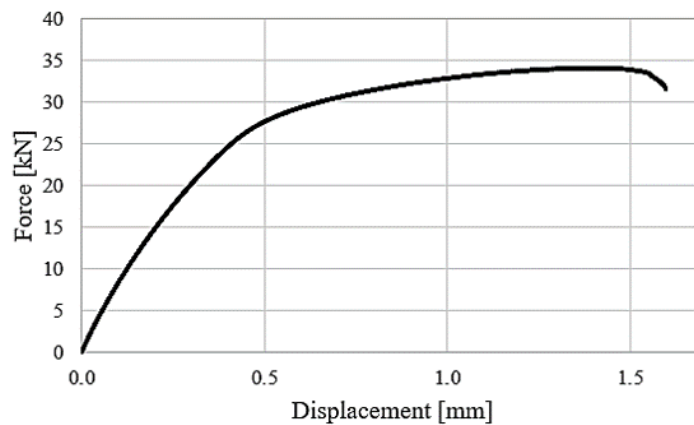
Figure 6.3: Static force versus displacement curve for V-notched specimen.

6.2.1 Ramberg-Osgood

The Ramberg-Osgood model (6), was fitted to the combination of strain gauge data and the force versus displacement tensile data with the engineering stress-strain curve seen in figure 6.4. The fit was done of the data from the plastic area, at some distance away from yield until necking started.
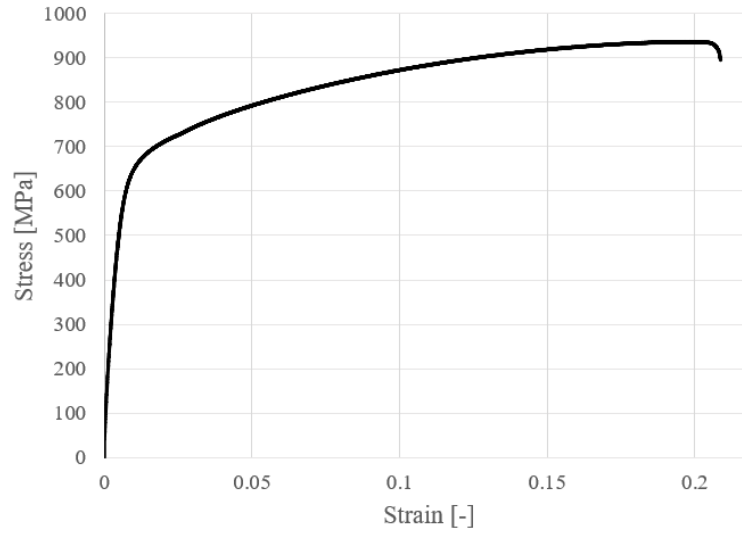
Figure 6.4: Engineering stress-strain curve with last part of curve fitted from displacement data.

Material properties obtained from the tests are listed in table 11. σ_y was obtained from where the curve deviated from the linear elastic area.

E	σ_y	$\sigma_{0.2\%}$	σ_{uts}	ϵ_n	n	K
$[GPa]$	$[MPa]$	$[MPa]$	$[MPa]$	$[-]$	$[-]$	$[MPa]$
143	650	549	940	0.2	0.1183	1154

Table 11: Material parameters obtained from tensile tests.

A graphic comparison of the fit between the power law data and stress-strain curve is shown in figure 8.2.

6.3   ABAQUS model

The analysis was performed using ABAQUS Complete Abaqus Environment (CEA). The model was drawn as a shell, according to plane condition, of one quarter of the model of the V-notch design seen in figure 6.5. Only the Young's modulus and the Poisson's ratio of the material properties was needed to do the linear elastic analysis. The material properties used was the Young's modulus of $200000 MPa$ and the Poisson's ratio ($\nu = 0.3$) for room temperature, a simplification from $\nu = 0.294$ reported in table 9.
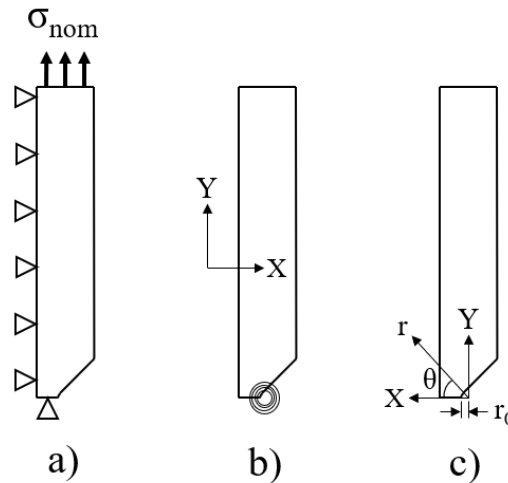
Figure 6.5: a) Boundary conditions and applied stress. b) Abaqus coordinate system for FE-analysis with partition geometry near notch tip. c) Stress coordinate system along notch bisector line to assess σ_θ.

All analysis was performed with boundary conditions according to figure (6.5 a) and with a negative pressure on the top edge of $1 MPa$, giving a higher stress on the net area on the notch bisector line given in table 12.

Notch	Stress on net area [MPa]
Unnotched	1.667
V-notch	2.577

Table 12: Pressure on the notch bisector line (net area) of the specimen analysis in Abaqus.

The simulation was performed using the mesh type CPE8: An 8-node bi-quadratic plane strain quadrilateral. All analysis where performed with "plane strain".

6.3.1   ABAQUS - SED

The function "partition geometry" made it possible to analyze both energy and volume on several small areas with different radii. The figure 6.6 show the mesh for the analysis of strain energy. Results of the analysis is shown in figure 6.12, where the analysis was compared to the parameters from the tensile test which decided the area of SED and thereby also the radius, R_0.
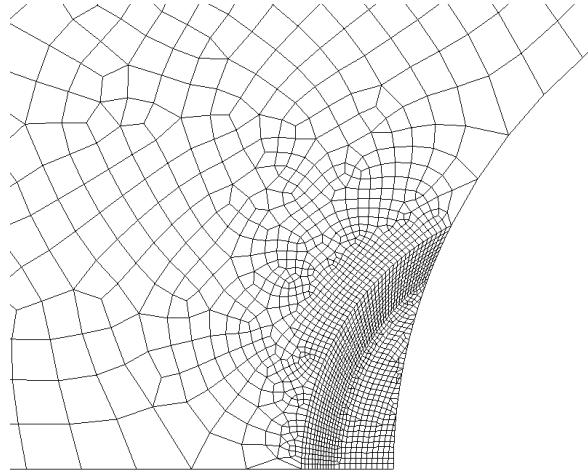
Figure 6.6: Mesh used for analysing strain energy density in ABAQUS.

6.3.2   ABAQUS - stress field

One quarter of the specimen was sketched and meshed with focus on fine mesh at the tip of the notch. Figure 6.7 below show an example of the mesh in the analysis. The numerical analysis of the stress field in ABAQUS was used to derive the notch sensitivity factor, K_t, for the V-notch member with results shown in figure 6.8 and 6.9. It was also used to derive the elastic and plastic NSIF in figure 6.10 and 6.11.
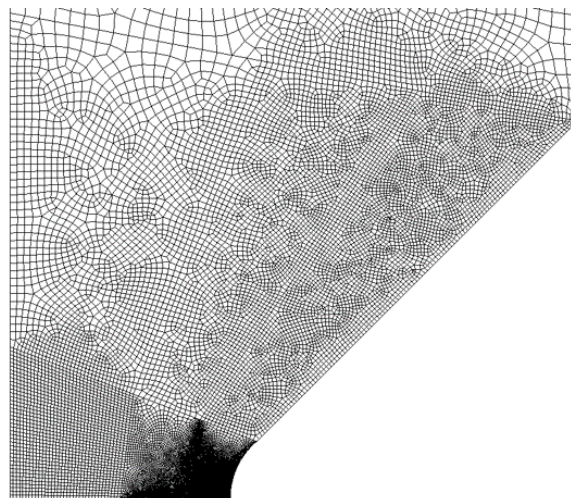
Figure 6.7: Mesh used for analysing K_t in ABAQUS.

6.4 Analytical approach to determine stress fields

In the presence of a notched member under traction loading, the maximum stress at the notch tip can be derived given the assumption that $r = r_0$ and that $\theta = 0$ by Lazzarin et al. [24]. This gives the following general equation for solving the σ_θ for mode 1 loading:

$$\sigma_\theta = \frac{\sigma_{max}}{4}\left(\frac{r}{r_0}\right)^{\lambda_1 - 1}\left[((1 + \lambda_1)\cos[(1 - \lambda_1)\theta])\right.$$
$$+ X_1(1 - \lambda_1)\cos[(1 + \lambda_1)\theta] \tag{60}$$
$$\left. + \left(\frac{r}{r_0}\right)^{\mu_1 - \lambda_1}[(3 - \lambda_1) - X_1(1 - \lambda_1)]\cos[(1 + \mu_1)\theta]\right].$$

Where X_1 is determined using the equation 61.

$$X_1 = -\frac{\sin[(1 - \lambda_1)\frac{q\pi}{2}]}{\sin[(1 + \lambda_1)\frac{q\pi}{2}]} \tag{61}$$

For a V-notch with $2\theta = 90^o$ and a notch tip radius of $\rho = 1mm$ this equation is shortened to:

$$\sigma_\theta = 0.152\sigma_{max}r^{-0.456}(2.383 + 0.609r^{-0.889}) \tag{62}$$

With r_0, λ_1 and μ_1 given in table 14. The analytically determined stress field is compared to that obtained using FEM in figure 6.9 where the elastic stress concentration factor is obtained by $K_{tnet} = \sigma_\theta / \sigma_{nom}$, see figure 6.8. The same value of K_t was obtained in the article by Solberg et al. [80]. When regarding the gross section area, the stress concentration factor becomes $K_{tgross} = \sigma_\theta / \sigma_{gross}$, being valid the expression $K_{tgross} = K_{tnet}(w_1/w_2)$. Values used in calculations in table 9.
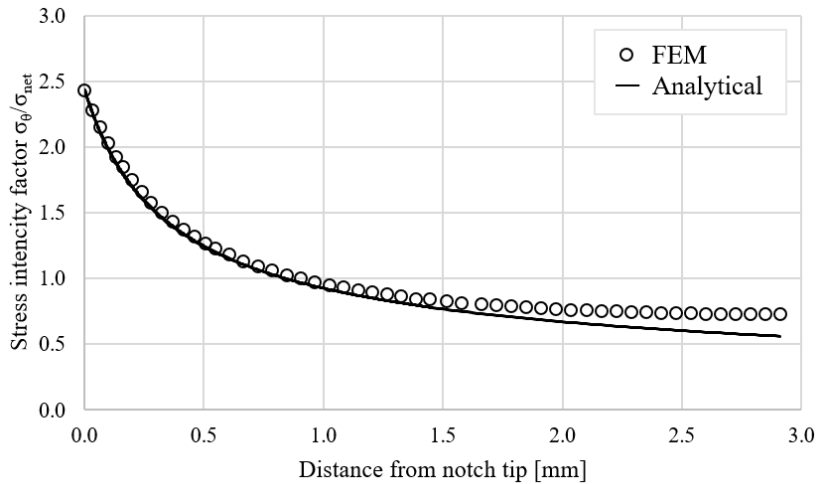
Figure 6.8: Stress intensity factor from equation of analytical stress field 62 and FE data.
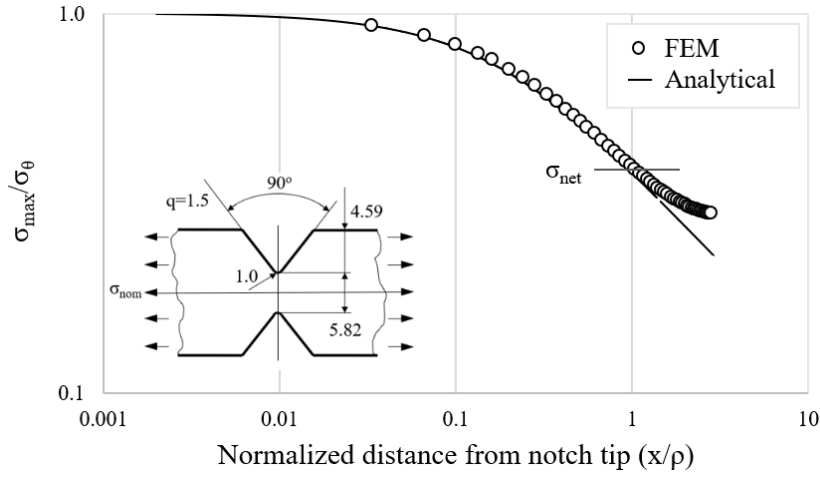
Figure 6.9: A comparison of numerical data and the analytical estimations of stress field with normalized distance in log-log scale.

The NSIF is calculated using equation 63 [81] where the stress field σ_θ is calculated from the stress field obtained through FE analysis . X is the distance from the notch tip on the notch bisector line $(x = r - r_0)$.

$$K_1 = \sqrt{2\pi}(r_0 + x)^{1-\lambda_1} \frac{(\sigma_\theta)_{\theta=0}}{1 + \omega_1 \left(\frac{r_0+x}{r_0}\right)^{\mu_1-\lambda_1}} \tag{63}$$

The value of NSIF is given according to normalized distance $(r - r_0)/\rho$ with the values obtained in figure 6.10. Where the value used in calculations was: $K^V_{\rho,I}/\sigma_{nom} = 5.3$.
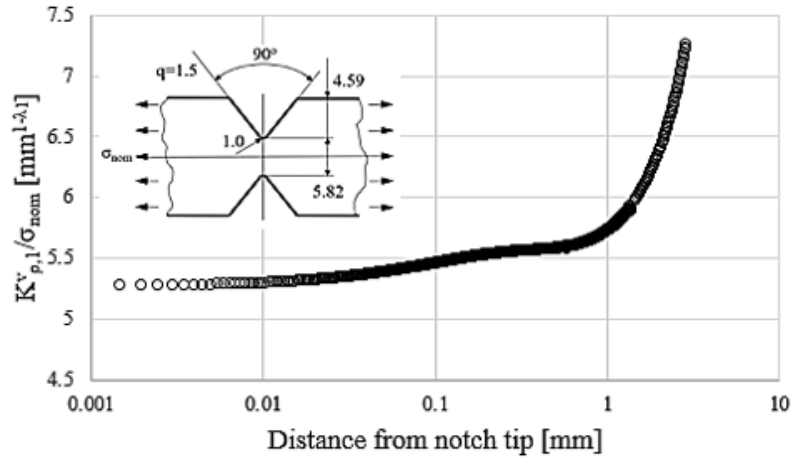
Figure 6.10: Notch sensitivity intensity factor based on numerically obtained stress field according to equation 63. Distance in log scale.

The plastic NSIF was calculated with values obtained from [35], for plane strain conditions. The equations is for sharp V-notches. Only the P-NSIF values calculated from equation 57 was used in calculation of SED. P-NSIF's are graphically displayed in figure 6.11.
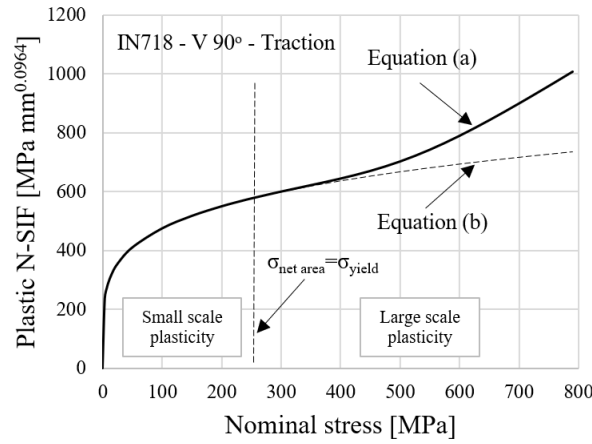
Figure 6.11: Plastic notch sensitivity intensity factor based on numerically obtained stress field according to equation (a) 57 and (b) 58.

6.5 Static SED analysis

Some of the necessary material properties is obtained from relevant literature, or extracted from the tensile test performed.

6.5.1 SED radius

The radius of the crescent shape of the SED area was determined by three different approaches and the values used are listed in table 13. The first approach determines the radius with the use of equation 31, or 32, depending on if the specimen is in either in plane stress or plane strain condition. An interpolation is needed when the condition is in between these two.

$$K_{c-strain} = 650 MPa \left(\frac{0.005m}{2.5} \right)^{\frac{1}{2}} = 29.1 MPa \sqrt{m} \tag{64}$$

$$K_{c-stress} = 650 MPa (\pi 0.005m)^{\frac{1}{2}} = 81.5 MPa \sqrt{m} \tag{65}$$

Assuming a fracture toughness of $K_{IC} = 50 MPa \sqrt{m}$ gives a condition in between plane strain and stress condition.

$$R_{0s-strain} = \frac{(1+0.3)(5-8\cdot0.3)}{4\pi} \left(\frac{50 MPa \sqrt{m}}{942 MPa} \right)^2 = 7.58 \cdot 10^{-4} m \tag{66}$$

$$R_{0s-stress} = \frac{(5-3\cdot0.3)}{4\pi} \left(\frac{50 MPa \sqrt{m}}{942 MPa} \right)^2 = 9.19 \cdot 10^{-4} m \tag{67}$$

The interpolated value of R_0 is shown in table 13. The second method is by a calibration of the radius from two different notch designs based on a linear elastic finite element method model, compared to results from the physical test of the unnotched specimen, see figure 6.12 and equation 68. R_0 shown in table 13.
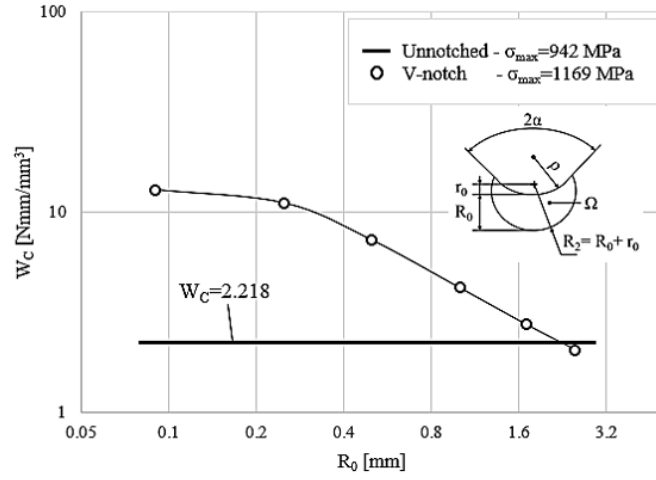
Figure 6.12: Calibrating R_0 with equation 68 in log-log scale.

$$\overline{W}_C = \frac{\sigma^2}{2E} \implies 2E = \frac{\sigma^2_{FEA}}{\overline{W}_{C-FEA}} = \frac{\sigma^2_{test}}{\overline{W}_{C-Test}} \tag{68}$$

A third method was used to determine the critical radius with an arbitrary shooting technique with radii between $0.01 - 1mm$ for the ductile critical SED value. This was because the SED from the numerical calibration was lower than this critical value, thereby making it impossible to determine this radius. Selected radius, R_0, is shown in table 13.

Approach	R_0 [mm]
Numerical	2.360
Analytical	0.822
Graphic	0.050

Table 13: Radius R_{0S} for SED analysis.

6.5.2 Calculation of SED

The approximation of the strain energy density was performed by different means in order to assess their different accuracy. Values for the the different parameters involved in the calculations are given in table 14 and . Parameters in between those given in the table was interpolated. The notched specimen was determined previously to be between plane strain and plane stress condition, but to simplify the calculations will now be assumed to be plane strain.

$2\alpha(^o)$	ρ[mm]	r_0[mm]	q	λ_1	μ_1	$\tilde{\omega}_1$	e_1	X_1
90	1	0.3333	1.5000	0.5445	-0.3449	0.8100	0.1462	1.841

Table 14: Values for V-shaped notches with $\nu = 0.3$ and plane strain conditions [81].

Calculation of SED based on NSIF is given in equation 35, for sharp V-notches and plane strain conditions. It was compared to equation 39 for blunt V-notches.

Values of necessary parameters are given in 13 and 14, with parameter H in figure 6.13 according to [28].
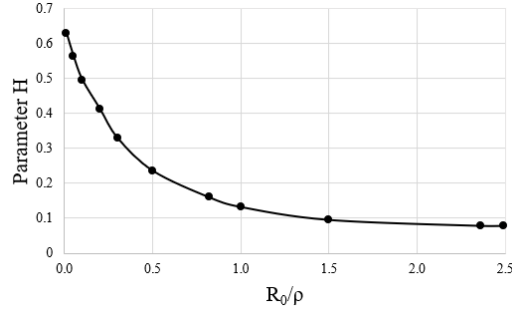
Figure 6.13: Parameter, H, for opening angle $2\alpha = 90^o$ and $\nu = 0.3$. Values beyond 1.0 are based on the linear trend.

The P-NSIF is determined under the hypothesis that the amount of energy concentration is equal under elastic and plastic conditions already stated based on the NSIF. The P-NSIF's are calculated by equation 57 for sharp V-notches. An approximate equation for blunt V-notches was made by simply introducing the difference between the equation for sharp and blunt V-notches by the use of NSIF as seen below in equation 69.The result of these are compared in the discussion.

$$\overline{W}^P_{modified}(R) = \frac{H\left(2\alpha, \frac{R_0}{\rho}\right)}{e_1} \cdot \frac{n}{(n+1)H^n} \cdot \frac{I_p(\gamma,n)}{\gamma(2-s(n+1))} \cdot \left(\frac{K^N_{1p}}{R^s_0}\right)^{n+1} \quad (69)$$

$2\alpha(^o)$	γ/π(rad)	$I_e(\gamma)$	$I_p(\gamma,n)$
90	3/4	0.7504	2.200

Table 15: Values of the integrals I_e and I_p under plane strain conditions. Determined for $\nu = 0.3$ and inverse strain hardening exponent $(1/n) = 8.45$, for blunted V-shaped notches [35].

Plastic integral was obtained from values listed in [35] and graphically displayed in figure 6.14 for sharp V-notches.
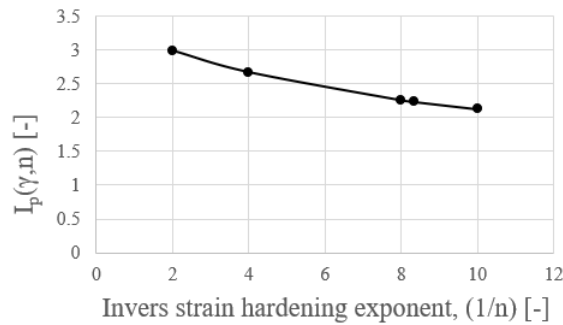
Figure 6.14: Plastic integral versus the strain hardening exponent. With $\nu = 0.3$ and $2\alpha = 90^o$.

6.5.3 Critical SED

One of the goal's of this thesis is to compare different failure criteria from the most basic to a model based on the Ramberg-Osgood material hardening properties obtained from the tensile test of the unnotched specimen.
Never the less the most used failure criteria used in strain energy density criterion is 6.5.3, which is known to give good accuracy when the failure is brittle or quasi-brittle [8].

$$W_{C-brittle} = \frac{\sigma_{uts}^2}{2E}$$

By the use of the same failure criteria as in the equivalent material concept criteria where critical SED is based on the traction stress-strain curve fitted to the Ramberg-Osgood relation in equation 6. This gives the ductile critical SED in equation 70 [31].

$$W_{C-ductile} = \frac{\sigma_y^2}{2E} + \frac{H}{n+1}\left[(\epsilon_{u,True})^{n+1} - (0.002)^{n+1}\right] \tag{70}$$

These failure criteria will be compared to simplified models seen in figure 6.15 b) and 6.15 c) where all the critical SED values are graphically displayed. Values used from the models are listed in table 16.
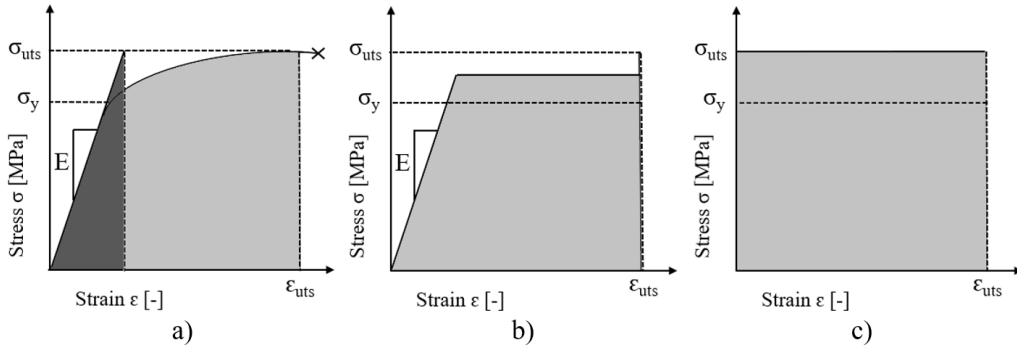
Figure 6.15: Different failure criteria models. a) Dark grey: brittle, light gray: strain hardening. b) Elastic-perfectly plastic. c) Perfectly plastic. Note: Not size comparable.

By means of	$W_C[Nmm/mm^3]$
Brittle	2.218
Elastic-perfectly plastic	160.8
Strain hardening	170.5
Perfectly plastic	188.4

Table 16: Failure criteria and their critical SED values.

7 Results

Table 17 show all of the estimated failure forces with the different strain energy density calculation methods and different failure criteria.

Notch	$\overline{W}$	Radius	Failure SED $W_C [Nmm/mm^3]$			
			2.218	160.8	170.5	188.4
Shape	By means of	R_0 [mm]	Failure force $[kN]$			
Sharp	NSIF (35)	0.050	-	53.9	57.0	58.4
		0.822	22.7	-	-	-
		2.360	36.9	-	-	-
Sharp	P-NSIF (53)	0.050	-	39.0	39.5	40.2
		0.822	22.5	-	-	-
		2.360	32.8	-	-	-
Blunt	NSIF (39)	0.050	-	27.4	28.3	29.8
		0.822	21.6	-	-	-
		2.360	52.1	-	-	-
Blunt	P-NSIF (69)	0.050	-	26.7	27.3	28.4
		0.822	21.5	-	-	-
		2.360	38.6	-	-	-

Table 17: Estimated failure force. Critical radius of $0.05mm$ was determined as a good approximation shown in figure 8.7.

Deviation from the experimental result are shown in table 18 with the experimental failure force of $34.02kN$.

Notch	$\overline{W}$	Radius	Failure SED $W_C [Nmm/mm^3]$			
			2.218	160.8	170.5	188.4
Shape	By means of	R_0 [mm]	Deviation from exp. [%]			
Sharp	NSIF (35)	0.050	-	58.5	67.4	71.6
		0.822	-33.3	-	-	-
		2.360	8.4	-	-	-
Sharp	P-NSIF (53)	0.050	-	14.7	16.0	18.3
		0.822	-33.8	-	-	-
		2.360	-3.5	-	-	-
Blunt	NSIF (39)	0.050	-	-19.3	-16.9	-12.5
		0.822	-36.4	-	-	-
		2.360	53.1	-	-	-
Blunt	P-NSIF (69)	0.050	-	-21.4	-19.6	-16.4
		0.822	-36.8	-	-	-
		2.360	13.3	-	-	-

Table 18: Deviation from experimental results.

With critical radius $R_0 = 0.05mm$ all equations except for sharp V-notches with the use of NSIF had accuracy within $\pm21.4\%$ of the failure force. Both the equations, NSIF and P-NSIF, for blunt notches underestimates the failure force while the equations for sharp notches overestimates it.

8   Discussion

8.0.1   Material properties

The material parameters obtained showed a good correlation to that values already reported in the literature. ASTM E8 though was not fully met because there was no length measurement being made before and after testing. The Young's modulus was derived by line fitting of the tensile data to approximately $143GPa$. A value lower than that of HT IN718, see table 7, but was similar to the value obtained by for example Popovich et al. [72] compared in figure 8.1. Elongation exceeded that tested by Popovich with elongation over 20% in both tensile tests of the unnotched specimen.
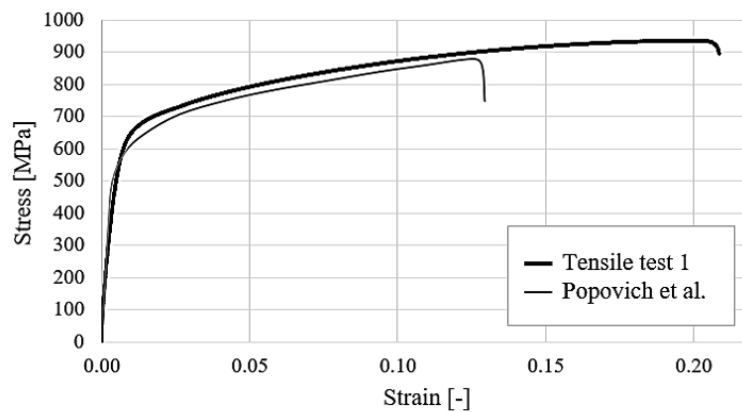
Figure 8.1: Comparison of tensile test data.

The speed of which the test was conducted was performed by error and trial. It may have affected the strength of the V-notched specimen that the speed was to great, giving that failure happened within two minutes ($0.8mm/min$). However Baufeld et al. [64] reported no evident dependency of strain rate on unnotched specimen produced by SMD and the notch strengthening factor was similar to that of En3B steel in [82]. The power fit with equation 6 is shown in figure 8.2 with good agreement, but slightly underestimating the stress close to yield.
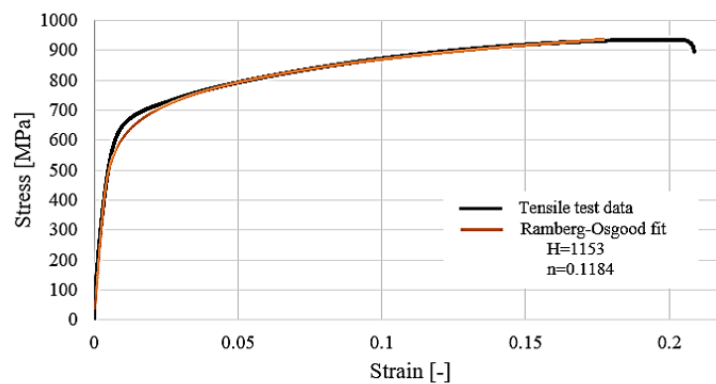
Figure 8.2: Ramberg-Osgood fit with tensile stress-strain curve of unnotched data. Values from table 9.

Critical for the estimation of SED was determining an appropriate fracture toughness. It determines the critical radius in the analytical approach together with σ_{uts} and ν. No or few data are given on the fracture toughness on IN718 members produced by AM not conducted to heat treatments. An assumption was made that the fracture toughness might be lower than for conventional manufacturing methods because of an earlier initiation of stable crack growth in studies performed by Konečná et al. [77]. AM specimen are also known to have higher porosity and coarser surface finish than by conventional manufacturing, as well as possible residual stress at perturbations. A fracture toughness of $50 MPa\sqrt{m}$ was assumed also based on values obtained in [52] of $62.5 MPa\sqrt{m}$. This value would give it a condition between plane-strain and plane-stress according to 33 and 34. Something also the fracture surface indicated of the notched specimen with shear lips as well as a flat surface between them [10].

8.0.2 SEM

SEM showed that the unnotched specimens had dimples of ellipse-shape and likely originate from the fracture of δ phases and show definitive signs of a ductile material in both specimen as seen in figure 8.3 a) of specimen test 1 [10]. Small pores can be seen in figure 8.3 b), between the contour- and hatching layers. Figure 8.3 c) show some shapes of possible striations or signs of print direction. Specimen in figure 8.3 d) had several cracks similar to that of J. Xu et al. [83], where the primary failure mode is transgranular fracture deformation. This specimen with the most distinct cracks failed at lower force.
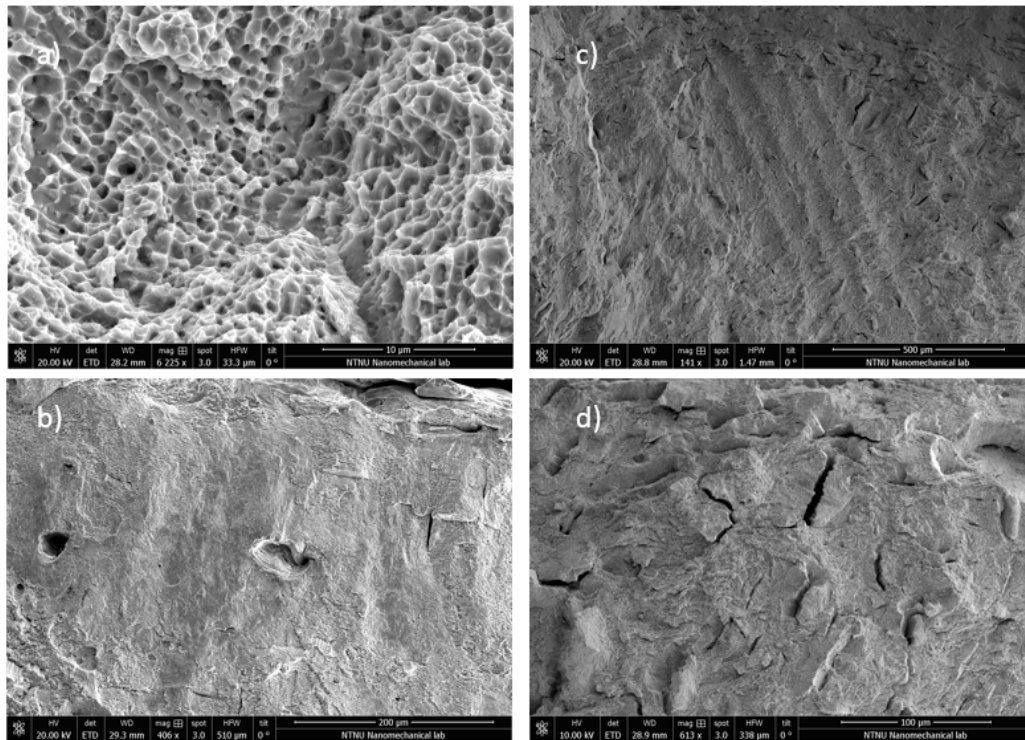
Figure 8.3: Unnotched specimen failure surface. a) and b) of test specimen 1. c) and d) of test specimen 2.

The V-notched specimen showed similar flaws as the unnotched specimens, where figure 8.4 a) show pores close to the surface. Figure 8.4 b) show similar cracks as in 8.3 d).
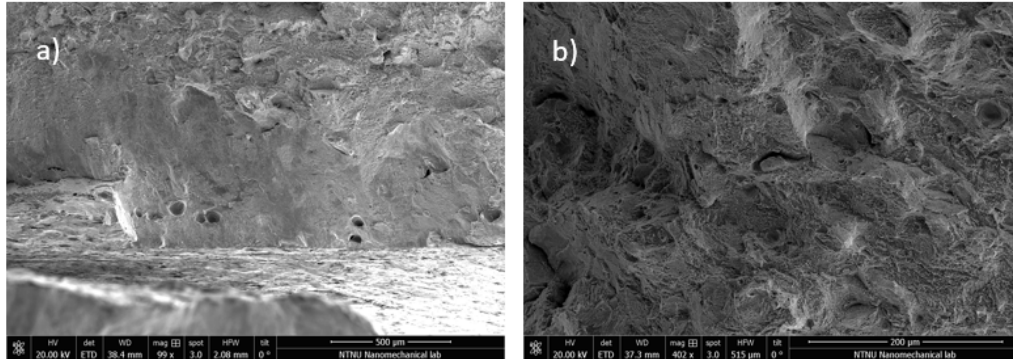
Figure 8.4: Blunt V-notch specimen failure surface. a) showing pores. b) showing cracks.

The fracture surface of the notched member had 45° inclining surfaces at both edges with flat surface in between, showing clear signs of a ductile material. The unnotched specimen failed at similar force.

8.0.3 SED calculations

The approach of estimating SED was based on a linear elastic model to determine their separate constitutive accuracy. Failure of the members was of course happening in the plastic regime in an ab-linear manner for the ductile IN 718. The goal was not to conduct any extensive plastic analysis, but to continue simplifying the approach to give a easy failure assessment also applicable for assessing AM geometries.

The stress field obtained from analytical analysis correlates well with that from the numerical analysis seen in figure 6.8 and gave the same value of the stress intensity factor as in Solberg et al [80]. Figure 6.9 show similar accuracy as reported by Lazzarin et al. in [24]. The stress fields was then used to calculate the NSIF, which is similar to values obtained by Lazzarin et al. in [84], with K_1/σ_{nom} of 5.3.

The analytically determined radius of $R_0 = 0.822mm$ is heavily influenced by the apparent fracture toughness of the material. Figure 8.5 suggest that a greater value of the fracture toughness would give more accurate results if the critical radius was between approximately $1 - 1.7mm$ obtained from equation 39.
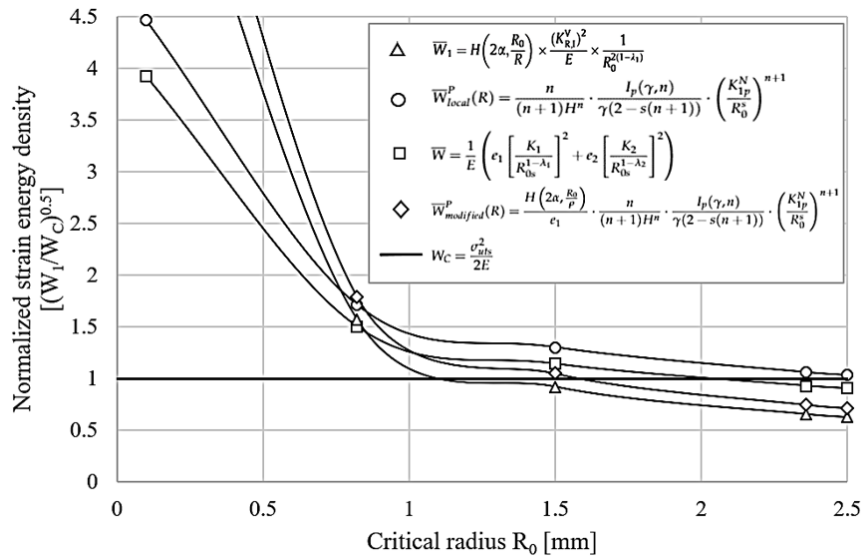
Figure 8.5: Critical radius obtained using three different calculating methods.

The numerically obtained radius of 2.360mm is almost covering all of the net area between the notches. Critical radii reported in [85] for Duraluminium of $R_0 = 1.382mm$ and $R_0 = 1.54mm$, and $R_0 = 0.53mm$ for AISI O1 from Strandberg et al. [86] are smaller than the radius obtained from the numerical analysis in Abaqus, but similar to that of the analytically obtained radius.
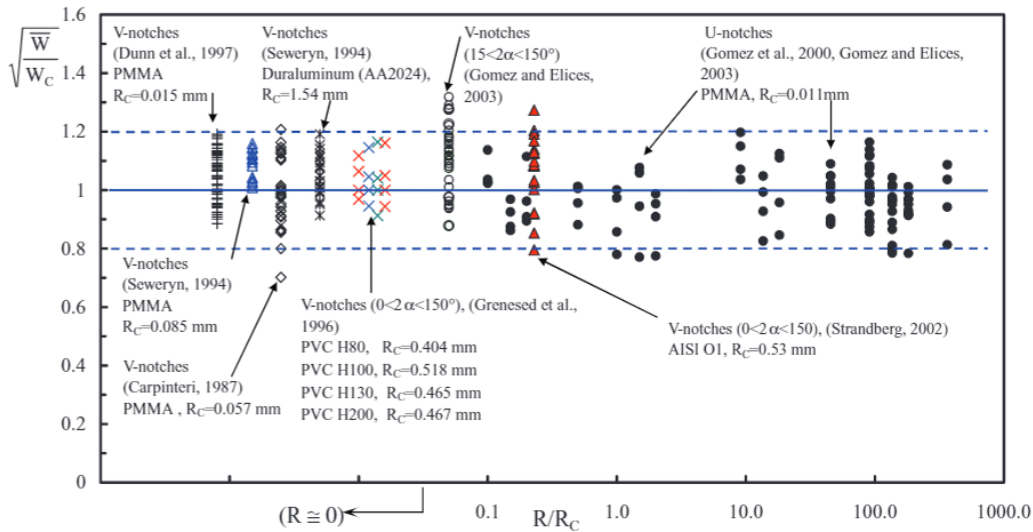
Figure 8.6: Static results from Lazzarin et al. [87] with critical radius.

The results from these test are not entirely comparable because the samples of Duraluminum had sharp V-notches and the AISI O1 steel was tested at temperature $T = -50.0^oC$ causing a more brittle failure. However, the experiments by Strandberg on AISI O1 steel still showed some contained plasticity and small rounding of the V-notch tip. Critical radius obtained from the shooting technique of $R_0 = 0.05mm$ was determined from figure 8.7, with the radius being the approximate closest fit for all four equations, when considering the ductile

failure criteria of $W_C = 170.5 Nmm/mm^3$. If only the blunt equations was considered, giving an radius of approximately $R_0 = 0.07mm$, could have given a more accurate assessment. This critical radius is however more comparable with the radii used for brittle materials such as PMMA fro Lazzarin et al. [87].
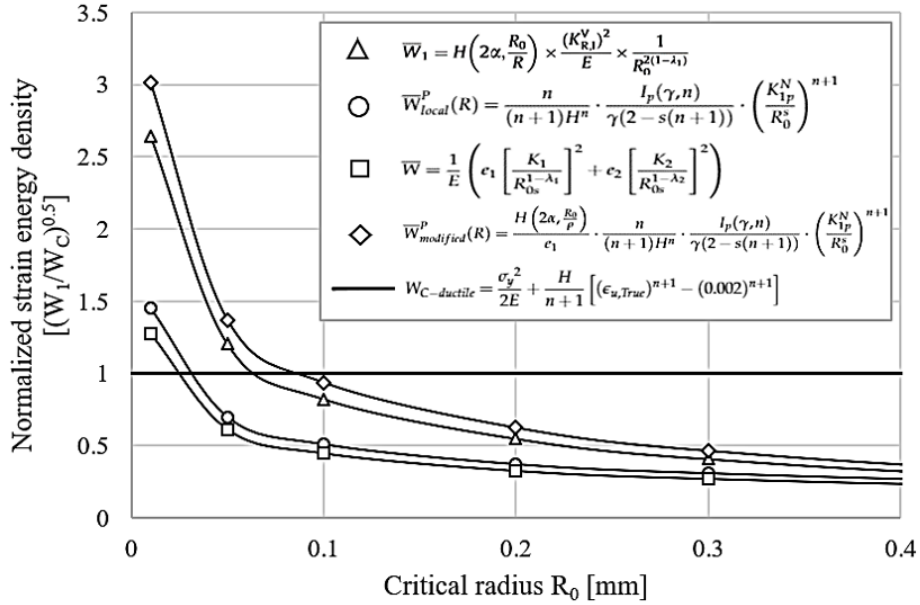
Figure 8.7: SED versus nominal stress, showing all four calculation methods with critical SED at $170.5 Nmm/mm^3$.

Equation 69 derived in this thesis for blunt P-NSIF give a reasonable outcome compared to the difference between the sharp equations for NSIF and P-NSIF. The SED value from the blunt P-NSIF have similar SED value with blunt NSIF until a nominal stress of approximately $300 MPa$ where it start to deviate from values of the blunt NSIF as seen in figure 8.8. The calculations of SED are assumed to be correct by the fact that the calculation method based on NSIF and P-NSIF are different, but gives the same SED value up to a certain stress.
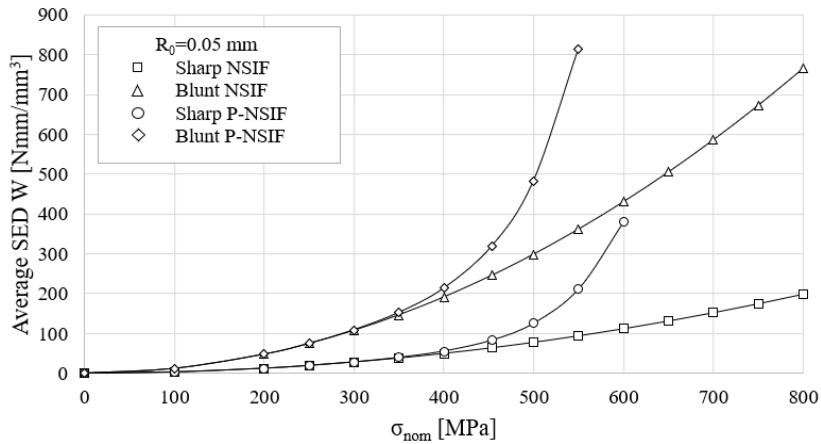
Figure 8.8: SED versus nominal stress of the four fundamental equations, with $R_0 = 0.05mm$.

8.0.4 Accuracy of failure prediction

The analytically obtained radius $R_0 = 0.822mm$, seen in figure 8.9 give the smallest scatter combined with the brittle failure criteria. But these methods highly underestimates the failure force of up to 37%. The failure criteria calibration proposed by Seweryn et al. [85] was not considered. He recommended to substitute σ_{uts} to "the maximum normal stress existing at the edge at the moment preceding the cracking", when unnotched specimens exhibit a non-linear behaviour whereas the behaviour of notched specimens remains linear. The SED at failure for the equation for blunt V-notch using NSIF of $\overline{W}_1 = 5.466Nmm/mm^3$ was close to the critical SED for the Duraluminum in Lazzarin et al. [23], where the maximum average SED was $\overline{W}_1 = 5.257Nmm/mm^3$.

The brittle failure criteria combined with the critical radius of $R_0 = 2.360mm$ derived from numerical analysis gives a good approximation for both of the equations for sharp V-notch, within range of -3.5 to 8.4%. The blunt equations overestimates the force with $13.3 - 53.1\%$.

The most reliable method seems to be the use of blunt approximation of SED for both NSIF and P-NSIF with the radius calibrated by the shooting technique seen in figure 8.7, highlighted by the circle. These methods slightly underestimate the failure force by a margin of 20% and less. However, the notch strengthening effect may cause a high discrepancy in ductile materials.
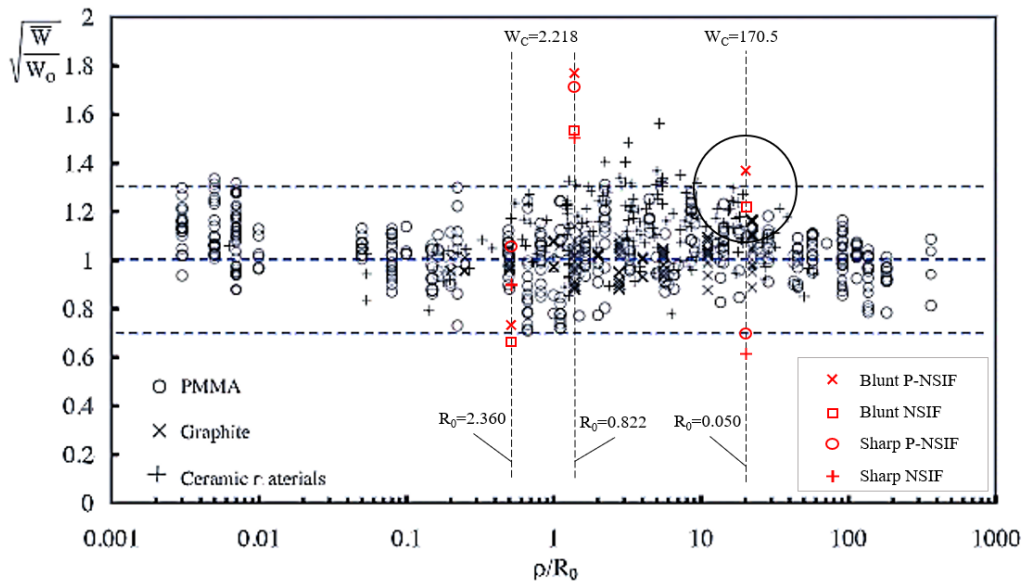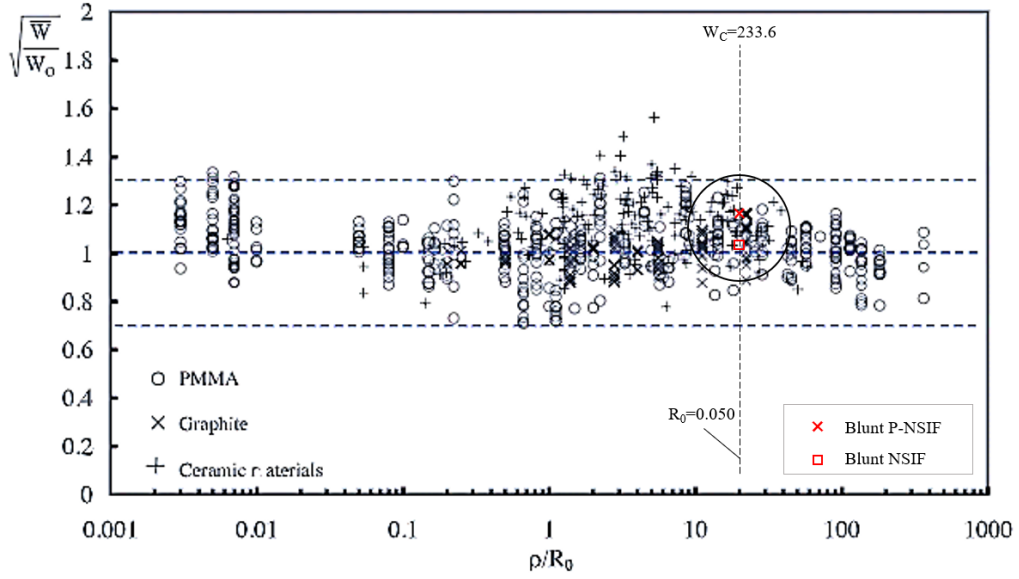

Figure 8.9: Synthesis of the data from all ceramic, graphite and PMMA specimens performed by Berto et al. [26], compared with results from this thesis.

Other assessments have been made in the passed where a ductile material has been thought of as brittle, such as in Glinka et al. [32] and Torabi et al. [31] as well as the TCD. Though the use of TCD is a crude estimate with no calibration of the efficient stress. The efficient stress can be derived by experimental tests of different notch geometries together with linear numerical analysis of the stress fields of these [88]. Lazzarin et al. [23] saw after several analyses of plastically deformable Duraluminum under plane strain condition, that a material obeying

a power hardening law had similar average value of the local energy as materials with linear elastic behavior.

Reported accuracy of static failure by use of linear elastic TCD is $\pm 15 - 20\%$ in Madrazo et al. [88] but was overestimating the failure force for bigger radii. EMC combined with SED was reported with the same accuracy and overestimation with larger radii [89]. An accuracy at approximately 12% with elasto-plastic analysis was reported by Alena et al. [90]. This is similar values obtained from this work, however compared to the TCD criteria, the SED criteria have multiple advantages. TCD needs very refined mesh in order to assess the stress field in the vicinity of the notch in a satisfying degree. SED on the contrary is mesh insensitive as already reviewed and it also includes the scale effect in the NSIF and P-NSIF [23].

8.0.5 Notch strengthening effect

The notch strengthening effect in SLM IN718 was significant with failure stress for the notched specimen at $1169 MPa$ compared to the unnotched ultimate tensile strength of $942 MPa$. Qu et al. [91] presented in their article a notch strength ratio (NSR) which is determined by the ratio of the ultimate tensile strength of the notched specimen divided with the unnotched ultimate tensile strength seen in equation 71. $NSR >> 1$ means notch strengthening. The ratio for the given samples in this article was 1.24, similar to that tested by Torabi et al. [82] at 1.26 of the En3B steel. The specimen from Torabi's report was a tensile tested double notch, with radius of $0.1mm$, $t = 6mm$, $2\alpha = 60^o$, giving a different notch intensity factor than of the v-shaped specimen of this thesis.

$$NSR = \frac{M}{K_t} = \frac{\sigma_{uts-unnotched}}{\sigma_{uts-notch}} \tag{71}$$

Where M is a an approximate material property and can be derived from 72.

$$M = \frac{1}{n\sqrt{(4k\alpha^2 + (1-k)^2)}} \tag{72}$$

Materials with a decreased α often have enhanced ability to plastically deform and also show an increased resistance to normal cleavage fracture.

8.0.6 Suggested failure criteria

Calibrating the critical failure criteria with the NSR could give a better approximation of failure. This would be equivalent to that of the calibration of σ_{eff} in TCD, where also the notch strengthening effect is included. Multiplying the NSR with the strain hardening criteria of $170.5 Nmm/mm^3$, and to the perfectly plastic criteria of $188.4 Nmm/mm^3$, together with the equations for blunt V-notches 39 and 69 gives a better approximation with accuracy in table 19:

	$\overline{W}$		Failure SED $W_C[Nmm/mm^3]$
By means of	Equation	211.4	233.6
NSIF	(39)	-7.8	-3.4
P-NSIF	(69)	-12.2	-8.9

Table 19: Accuracy with NSR calibrated failure criteria and $R_0 = 0.05mm$ and equations for blunt V-notches.

The discrepancy can be seen in figure 8.10, with the results highlighted in the circle. Results from these are highly accurate.

Figure 8.10: Synthesis of the data from all ceramic, graphite and PMMA specimens performed by Berto et al. [26], compared with new failure criteria.

With this calibration it may offer a better approximation of failure assessment. But further testing is needed to validate the result for different materials and notch geometry. The suggested new failure criteria for ductile materials under static Mode I tensile conditions is stated as:

$$W_C = \sigma_{uts}\epsilon_n\frac{M}{K_t} \tag{73}$$

9 Conclusion

In this thesis the accuracy of different methods of static failure of a notch geometry were investigated using strain energy density. The specimen, made of Inconel 718, was produced by selective laser melting without any after treatment. Topics such as structural integrity, theory of critical density, strain energy density, additive manufacturing and material properties of AM Inconel 718 were investigated.
General conclusion:

- The full advantage of the mechanical properties of IN 718 produced by conventional or additive manufacturing can only be achieved with heat treatments.

- Additive manufacturing offers geometry complexity that is not achievable by means of conventional manufacturing.

- Porosity in additive manufactured components can be decreased by means of hot isostatic pressing.

- Fatigue strength of additive manufactured IN718 with no after treatment is reported to be 26% of the ultimate tensile strength, compared to approximately 34% for conventional manufacturing.

- Ductility decreases by HT and increases by HIP.

Answers to research questions:

What is the static mechanical properties of additive manufactured IN 718?

- AM IN 718 shows anisotropy.

- Static properties of heat treated AM IN 718 at room temperature are almost comparable to those of CM.

- Static properties at room temperature of AM IN 718 which was treated HT and HIP are comparable to those of CM.

- Static properties at $650^o C$ of AM IN 718 which was treated with HT and HIP are comparable to those of CM.

- AM IN 718 crack growth threshold is lower than that of CM.

- Hardness of AM IN 718 by HT and HIP is comparable to that of CM.

Is it possible to give accurate estimations of static failure of AM IN 718 with blunt notch geometry, based on different calculation methods of the strain energy density criterion with equations for sharp and blunt V-notches using NSIF and P-NSIF, when the failure criterion is based on brittle, ductile or simplified ductile materials?

- The equations for blunt V-notch with NSIF and P-NSIF give an underestimation within acceptable limits of 12.5% and 16.4%, respectively.

- The approach of graphically determined critical radius of $R_0 = 0.050mm$ gives the most accurate estimate with the equations for blunt V-notches.

- The perfectly plastic model with critical SED of $188.4 Nmm/mm^3$ gives the most accurate estimate of the failure force.

- Equations for sharp V-notches are not suitable for estimating the failure force of blunt V-notched geometries.

Further work:

- To validate accuracy of SED calculation of blunt notches with both the use of elastic and plastic notch sensitivity intensity factor for other materials and notch shapes.

- To validate the suggested failure criterion on other materials and notch geometries.

- To validate the accuracy of both SED calculations and suggested failure criteria for mixed mode loadings.

References

[1] Andrzej Nowotnik. "Nickel-Based Superalloys". In: Dec. 2016. ISBN: 9780128035818. DOI: 10.1016/B978-0-12-803581-8.02574-1.

[2] Daniel F. Paulonis and John J. Schirra. "Alloy 718 at Pratt Whitney - Historical perspective and future challenges". In: (2001). URL: https://www.tms.org/superalloys/10.7449/2001/Superalloys_2001_13_23.pdf.

[3] *http://www.specialmetals.com/assets/smc/documents/inconel$_a$lloy$_7$18.pdf*. Sept. 2007.

[4] *https://www.phase-trans.msm.cam.ac.uk/2003/Superalloys/superalloys.html*. June 2018.

[5] Harlal Mali and Deepak Unune. "Machinability of Nickel-Based Superalloys: An Overview". In: Jan. 2017. ISBN: 9780128035818. DOI: 10.1016/B978-0-12-803581-8.09817-9.

[6] Miguel et al. Seabra. "Selective laser melting (SLM) and topology optimization for lighter aerospace componentes". eng. In: *Procedia Structural Integrity* 1 (2016), pp. 289–296. ISSN: 2452-3216.

[7] Christian Lindemann et al. "Analyzing Product Lifecycle Costs for a Better Understanding of Cost Drivers in Additive Manufacturing". In: Aug. 2012.

[8] F. Berto and P. Lazzarin. "A review of the volume-based strain energy density approach applied to V-notches and welded structures". eng. In: *Theoretical and Applied Fracture Mechanics* 52.3 (2009), pp. 183–194. ISSN: 0167-8442.

[9] Paolo Lazzarin, Filippo Berto, and Michele Zappalorto. "Rapid calculations of notch stress intensity factors based on averaged strain energy density from coarse meshes: Theoretical bases and applications". eng. In: *International Journal of Fatigue* 32.10 (2010), pp. 1559–1567. ISSN: 0142-1123.

[10] Norman E Dowling. *Mechanical behavior of materials : engineering methods for deformation, fracture, and fatigue*. eng. Upper Saddle River, N.J, 2007.

[11] Walter Ramberg and William Osgood. *Description of stress-strain curves by three parameters*. eng. 1943. URL: http://search.proquest.com/docview/21649446/.

[12] OH Basquin. "The Exponential Law of Endurance Tests". In: 10 (1910), pp. 625–630.

[13] H. Neuber. *Theory of Notch Stresses: Principles for Exact Calculation of Strength with Reference to Structural Form and Material*. Translation series. USAEC Office of Technical Information, 1961. URL: https://books.google.no/books?id=NUNGAAAAYAAJ.

[14] RE Petersen. "Notch Sensitivity". In: *Metal fatigue* (1959).

[15] S S Manson. *Behavior of Materials Under Conditions of Thermal Stress*. eng. 1954. URL: http://hdl.handle.net/2060/19930092197.

[16] M P. Gomez and W E. A. Anderson. "A Rational Analytic Theory of Fatigue". In: *Trend Engng.* 13 (Jan. 1961).

[17] Luca Susmel and David Taylor. "The Theory of Critical Distances to estimate the static strength of notched samples of Al6082 loaded in combined tension and torsion. Part II: Multiaxial static assessment". eng. In: *Engineering Fracture Mechanics* 77.3 (2010), pp. 470–478. ISSN: 0013-7944.

[18] L. Susmel and D. Taylor. "On the use of the Theory of Critical Distances to predict static failures in ductile metallic materials containing different geometrical features". eng. In: *Engineering Fracture Mechanics* 75.15 (2008), pp. 4410–4421. ISSN: 0013-7944.

[19] D. Taylor. "Predicting the fracture strength of ceramic materials using the theory of critical distances". eng. In: *Engineering Fracture Mechanics* 71.16 (2004), pp. 2407–2416. ISSN: 0013-7944.

[20] L. Susmel and D. Taylor. "A novel formulation of the theory of critical distances to estimate lifetime of notched components in the medium cycle fatigue regime". In: *Fatigue Fracture of Engineering Materials Structures* 30.7 (2007), pp. 567–581. ISSN: 8756-758X.

[21] M. H. El Haddad, K. N. Smith, and T. H. Topper. "Fatigue Crack Propagation of Short Cracks". eng. In: *Journal of Engineering Materials and Technology* 101.1 (1979). ISSN: 00944289.

[22] P. Lazzarin, R. Tovo, and G. Meneghetti. "Fatigue crack initiation and propagation phases near notches in metals with low notch sensitivity". eng. In: *International Journal of Fatigue* 19.8 (1997), pp. 647–657. ISSN: 0142-1123.

[23] P. Lazzarin and R. Zambardi. "A finite-volume-energy based approach to predict the static and fatigue behavior of components with sharp V-shaped notches". In: *International Journal of Fracture* 112.3 (Dec. 2001), pp. 275–298. ISSN: 1573-2673. DOI: 10.1023/A:1013595930617. URL: https://doi.org/10.1023/A:1013595930617.

[24] P. Lazzarin and R. Tovo. "A unified approach to the evaluation of linear elastic stress fields in the neighborhood of cracks and notches". In: *International Journal of Fracture* 78.1 (Mar. 1996), pp. 3–19. ISSN: 1573-2673. DOI: 10.1007/BF00018497. URL: https://doi.org/10.1007/BF00018497.

[25] B. Gross and A. Mendelson. "Plane elastostatic analysis of V-notched plates". In: *International Journal of Fracture Mechanics* 8.3 (Sept. 1972), pp. 267–276. ISSN: 1573-2673. DOI: 10.1007/BF00186126. URL: https://doi.org/10.1007/BF00186126.

[26] F. Berto and P. Lazzarin. "Recent developments in brittle and quasi-brittle failure assessment of engineering materials by means of local approaches". eng. In: *Materials Science Engineering R* 75.1 (2014), pp. 1–48. ISSN: 0927-796X.

[27] J. F Knott. *Fundamentals of fracture mechanics*. eng. London, 1973.

[28] P. Lazzarin and F. Berto. "Some Expressions for the Strain Energy in a Finite Volume Surrounding the Root of Blunt V-notches". eng. In: *International Journal of Fracture* 135.1 (2005), pp. 161–185. ISSN: 0376-9429.

[29] P. Lazzarin et al. "Some advantages derived from the use of the strain energy density over a control volume in fatigue strength assessments of welded joints". eng. In: *International Journal of Fatigue* 30.8 (2008), pp. 1345–1357. ISSN: 0142-1123.

[30] Robert D Cook. *Finite element modeling for stress analysis*. eng. New York, 1995.

[31] Ali Reza Torabi. "Estimation of tensile load-bearing capacity of ductile metallic materials weakened by a V-notch: The equivalent material concept". In: *Materials Science and Engineering: A* 536 (Feb. 2012), pp. 249–255. DOI: 10.1016/j.msea.2012.01.007.

[32] G Glinka. "Energy density approach to calculation of inelastic strain-stress near notches and cracks". In: *Engineering Fracture Mechanics* 22 (Dec. 1985), pp. 485–508. DOI: 10.1016/0013-7944(85)90148-1.

[33] Sergio Cicero et al. "Estimation of Fracture Loads in AL7075-T651 Notched Specimens Using the Equivalent Material Concept Combined with the Strain Energy Density Criterion and with the Theory of Critical Distances". eng. In: *Metals* 8.2 (2018). ISSN: 2075-4701. URL: http://search.proquest.com/docview/2014726663/.

[34] Krzysztof Molski and G Glinka. "A method of elastic-plastic stress and strain calculation at a notch root". In: *Materials Science and Engineering* 50 (Sept. 1981), pp. 93–100. DOI: 10.1016/0025-5416(81)90089-6.

[35] P Lazzarin and R Zambardi. "The Equivalent Strain Energy Density approach reformulated and applied to sharp V-shaped notches". In: *Fatigue Fracture of Engineering Materials Structures* 25 (Sept. 2002), pp. 917–928. DOI: 10.1046/j.1460-2695.2002.00543.x.

[36] P Lazzarin and R Tovo. "A notch intensity factor approach to the stress analysis of welds". In: *Fatigue Fracture of Engineering Materials Structures* 21.9 (1998), pp. 1089–1103. ISSN: 8756-758X.

[37] "Apparatus for production of three-dimensional objects by stereolithography". In: *Google patents* (1986). URL: http://www.google.com/patents/us4575330.

[38] G. Costabile et al. "Cost models of additive manufacturing: A literature review". eng. In: *International Journal of Industrial Engineering Computations* 8.2 (2016), pp. 263–283. ISSN: 1923-2926. URL: https://doaj.org/article/5b985a54117a4a71a32d76dcfa6a7fee.

[39] John J. Lewandowski and Mohsen Seifi. "Metal Additive Manufacturing: A Review of Mechanical Properties". eng. In: *Annual Review of Materials Research* 46.1 (2016), pp. 151–186. ISSN: 1531-7331.

[40] Chor Yen Yap et al. "Review of selective laser melting: Materials and applications". In: *Applied Physics Reviews* 2 (Dec. 2015), p. 041101. DOI: 10.1063/1.4935926.

[41] Jean-Pierre Kruth et al. "Part and material properties in selective laser melting of metals". In: *16th International Symposium on Electromachining, ISEM 2010* (Jan. 2010).

[42] N.L. Loh and K.Y. Sia. "An overview of hot isostatic pressing". In: *Journal of Materials Processing Tech.* 30.1 (1992), pp. 45–65. ISSN: 09240136.

[43] *http://www.kobelco.co.jp/english/products/ip/technology/hip.html*.

[44] H. V. Atkinson and S. Davies. "Fundamental aspects of hot isostatic pressing: An overview". In: *Metallurgical and Materials Transactions A* 31.12 (Dec. 2000), pp. 2981–3000. ISSN: 1543-1940. DOI: 10.1007/s11661-000-0078-2. URL: https://doi.org/10.1007/s11661-000-0078-2.

[45] M. G. Stout and W. W. Gerberich. "Structure/property/continuum synthesis of ductile fracture in inconel alloy 718". In: *Metallurgical Transactions A* 9.5 (May 1978), pp. 649–658. ISSN: 1543-1940. DOI: 10.1007/BF02659922. URL: https://doi.org/10.1007/BF02659922.

[46] *https://www.upmet.com/products/nickel-alloys/alloy-718*. June 2019.

[47] *https://www.espimetals.com/index.php/technical-data/91-Inconel%20718*. June 2019.

[48] *https://www.elgiloy.com/wire-inconel-alloy-718/*. June 2019.

[49] *https://www.farinia.com/additive-manufacturing/3d-materials/inconel-718-aerospace-additive-manufacturing*.

[50] R Rajendran et al. "Strain hardening exponents and strength coefficients for aeroengine isotropic metallic materials-a reverse engineering approach". In: *Journal of the Mechanical Behavior of Materials* 23 (Sept. 2014). DOI: 10.1515/jmbm-2014-0012.

[51] R. Cortes et al. "Fatigue and crack growth behavior of Inconel 718-AL6XN dissimilar welds". eng. In: *Materials Science Engineering A* 745 (2019), pp. 20–30. ISSN: 0921-5093.

[52] L.A James. "Fatigue-Crack Growth in Inconel 718 Weldments at Elevated Temperatures". In: (1978).

[53] G. Liu, David K. Rehbein, and Otto Buck. *Anisotropy of the Fracture Toughness in Aged Inconel 718*. Jan. 1997.

[54] L. Zhong et al. "High cycle fatigue performance of inconel 718 alloys with different strengths at room temperature". In: *Metals* 9.1 (2019). ISSN: 20754701.

[55] Juraj Belan. "The Fractography Analysis of IN 718 Alloy after Fatigue Test". eng. In: *Key Engineering Materials* 635 (2015), pp. 9–12. ISSN: 1013-9826.

[56] Yoshinori Ono et al. "High-cycle Fatigue Properties of Alloy718 Base Metal and Electron Beam Welded Joint". eng. In: *Physics Procedia* 67.C (2015), pp. 1028–1035. ISSN: 1875-3892.

[57] Xian-feng Ma et al. "Fatigue and fracture behavior of nickel-based superalloy Inconel 718 up to the very high cycle regime". eng. In: *Journal of Zhejiang University-SCIENCE A* 11.10 (2010), pp. 727–737. ISSN: 1673-565X.

[58] Kawagoishi, Chen, and Nisitani. "Fatigue strength of Inconel 718 at elevated temperatures". In: *Fatigue Fracture of Engineering Materials Structures* 23.3 (2000), pp. 209–216. ISSN: 8756-758X.

[59] Yoshinori Ono et al. "High-Cycle Fatigue Properties at Cryogenic Temperatures in INCONEL 718 Nickel-based Superalloy". eng. In: *MATERIALS TRANSACTIONS* 45.2 (2004), pp. 342–345. ISSN: 1345-9678.

[60] Izaro Ayesta et al. "Influence of the WEDM process on the fatigue behavior of InconelÂ® 718". eng. In: *International Journal of Fatigue* 92.P1 (2016), pp. 220–233. ISSN: 0142-1123.

[61] Kristin Morgan and Douglas Wells. *Overview of Fatigue and Damage Tolerance Performance of SLM Alloy 718*. URL: https://ntrs.nasa.gov/archive/nasa/casi.ntrs.nasa.gov/20160007853.pdf.

[62] L Xiao, Daolun Chen, and M Chaturvedi. "Effect of Boron on Fatigue Crack Growth Behavior in Superalloy IN 718 at RT and $650^{\circ}C$". In: *Materials Science and Engineering: A* 428 (July 2006), pp. 1–11. DOI: 10.1016/j.msea.2005.08.206.

[63] D.B. Witkin, D.N. Patel, and G.E. Bean. "Notched fatigue testing of Inconel 718 prepared by selective laser melting". In: *Fatigue and Fracture of Engineering Materials and Structures* (2018). ISSN: 8756758X.

[64] Bernd Baufeld. "Mechanical Properties of INCONEL 718 Parts Manufactured by Shaped Metal Deposition (SMD)". eng. In: *Journal of Materials Engineering and Performance* 21.7 (2012), pp. 1416–1421. ISSN: 1059-9495.

[65] P.L. Blackwell. "The mechanical and microstructural characteristics of laser-deposited IN718". eng. In: *Journal of Materials Processing Tech.* 170.1 (2005), pp. 240–246. ISSN: 0924-0136.

[66] Xiaoming Zhao et al. "Study on microstructure and mechanical properties of laser rapid forming Inconel 718". eng. In: *Materials Science Engineering A* 478.1 (2008), pp. 119–124. ISSN: 0921-5093.

[67] Joshua Hibberd and R. Keith Bird. *Tensile Properties and Microstructure of Inconel 718 Fabricated with Electron Beam Freeform Fabrication (EBF(sup 3)) - NASA/TM-2009-215929*. eng. Tech. rep. 2009. URL: http://hdl.handle.net/2060/20090033142.

[68] Wesley A. Tayon et al. "Correlation Between Microstructure and Mechanical Properties in an Inconel 718 Deposit Produced Via Electron Beam Freeform Fabrication". eng. In: *Journal of Manufacturing Science and Engineering* 136.6 (2014). ISSN: 1087-1357.

[69] Yi-Nan Zhang et al. "Tensile properties of laser additive manufactured Inconel 718 using filler wire". eng. In: *Journal of Materials Research* 29.17 (2014), pp. 2006–2020. ISSN: 08842914. URL: http://search.proquest.com/docview/1562776647/.

[70] H. Qi, M. Azer, and A. Ritter. "Studies of Standard Heat Treatment Effects on Microstructure and Mechanical Properties of Laser Net Shape Manufactured INCONEL 718". eng. In: *Metallurgical and Materials Transactions A* 40.10 (2009), pp. 2410–2422. ISSN: 1073-5623.

[71] X. Cao et al. "Effect of pre- and post-weld heat treatment on metallurgical and tensile properties of Inconel 718 alloy butt joints welded using 4kW Nd:YAG laser". eng. In: *Journal of Materials Science* 44.17 (2009), pp. 4557–4571. ISSN: 0022-2461.

[72] V.A. Popovich et al. "Impact of heat treatment on mechanical behaviour of Inconel 718 processed with tailored microstructure by selective laser melting". eng. In: *Materials Design* 131 (2017), pp. 12–22. ISSN: 0264-1275.

[73] Anatoly A Popovich et al. "Microstructure and Mechanical Properties of Inconel 718 Produced by SLM and Subsequent Heat Treatment". eng. In: *Key Engineering Materials* 651-653 (2015), pp. 665–670. ISSN: 1013-9826.

[74] *Overview of Fatigue and Damage Tolerance Performance of SLM Alloy 718*. June 2019. URL: https://www.upmet.com/products/nickel-alloys/alloy-718.

[75] Radomila Konecna et al. "Microstructure and directional fatigue behavior of Inconel 718 produced by selective laser melting". eng. In: *Procedia Structural Integrity* 2 (2016), pp. 2381–2388. ISSN: 2452-3216.

[76] K. Solberg, J. Torgersen, and F. Berto. "Fatigue Behaviour of Additively Manufactured Inconel 718 Produced by Selective Laser Melting." In: *Procedia Structural Integrity* 13 (2018), pp. 1762–1767. ISSN: 2452-3216.

[77] Radomila Konecna, Ludvik Kunz, and Gianni Nicoletto. "Fatigue crack growth behavior of Inconel 718 produced by selective laser melting". In: *International Journal of Fatigue* 10 (Mar. 2016), pp. 31–40. DOI: 10.3221/IGF-ESIS.36.04.

[78] M. Clavel and A. Pineau. "Fatigue behaviour of two nickel-base alloys I: Experimental results on low cycle fatigue, fatigue crack propagation and substructures". eng. In: *Materials Science and Engineering* 55.2 (1982), pp. 157–171. ISSN: 0025-5416.

[79] J. Yuen, P. Roy, and W. Nix. "Effect of oxidation kinetics on the near threshold fatigue crack growth behavior of a nickel base superalloy". eng. In: *Metallurgical Transactions A* 15.9 (1984), pp. 1769–1775. ISSN: 0360-2133.

[80] K. Solberg and F. Berto. "Notch-defect interaction in additively manufactured Inconel 718". In: *International Journal of Fatigue* 122 (2019), pp. 35–45. ISSN: 0142-1123.

[81] S. Filippi, P. Lazzarin, and R. Tovo. "Developments of some explicit formulas useful to describe elastic stress fields ahead of notches in plates". eng. In: *International Journal of Solids and Structures* 39.17 (2002), pp. 4543–4565. ISSN: 0020-7683.

[82] A.R Torabi. "Estimation of tensile load-bearing capacity of ductile metallic materials weakened by a V-notch: The equivalent material concept". eng. In: *Materials Science and Engineering, Part A (Structural Materials: Properties, Microstructure and Processing)* 536 (2012), pp. 249–255. ISSN: 0921-5093.

[83] Jinghao Xu, Zaiwang Huang, and Liang Jiang. "Effect of heat treatment on low cycle fatigue of IN718 superalloy at the elevated temperatures". eng. In: *Materials Science Engineering A* 690 (2017), pp. 137–145. ISSN: 0921-5093.

[84] P. Lazzarin and S. Filippi. "A generalized stress intensity factor to be applied to rounded V-shaped notches". eng. In: *International Journal of Solids and Structures* 43.9 (2006), pp. 2461–2478. ISSN: 0020-7683.

[85] Andrzej Seweryn. "Brittle fracture criterion for structures with sharp notches". eng. In: *Engineering Fracture Mechanics* 47.5 (1994), pp. 673–681. ISSN: 0013-7944.

[86] M Strandberg. "Fracture at V-notches with contained plasticity". eng. In: *Engineering Fracture Mechanics (UK)* 69.3 (2002), pp. 403–415. ISSN: 0013-7944. URL: http://search.proquest.com/docview/27142484/.

[87] P. Lazzarin et al. "Brittle failures from U- and V-notches in mode I and mixed, I + II, mode: a synthesis based on the strain energy density averaged on finite size volumes". In: *Fatigue Fracture of Engineering Materials Structures* 32.8 (2009), pp. 671–684. ISSN: 8756-758X.

[88] V. Madrazo, S. Cicero, and I.A. Carrascal. "On the Point Method and the Line Method notch effect predictions in Al7075-T651". eng. In: *Engineering Fracture Mechanics* 79 (2011). ISSN: 0013-7944.

[89] Juan Diego Fuentes et al. "Estimation of Fracture Loads in AL7075-T651 Notched Specimens Using the Equivalent Material Concept Combined with the Strain Energy Density Criterion and with the Theory of Critical Distances". eng. In: *Metals* 8.2 (2018). ISSN: 2075-4701. URL: https://doaj.org/article/640333b7737b4c80be8d47690dfbcbd3.

[90] Terekhina Alena et al. "Elasto-plastic TCD as a method of failure prediction". eng. In: *Procedia Structural Integrity* 5 (2017), pp. 569–576. ISSN: 2452-3216.

[91] Ruitao Qu, Peng Zhang, and Zhefeng Zhang. "Notch Effect of Materials: Strengthening or Weakening?" eng. In: *Journal of Materials Science Technology* 30.6 (2014). ISSN: 1005-0302.

[92] N.I Muschelisvilli. *Some basic problems of the mathematical theory of elasticity : fundamental equations, plane theory of elasticity, torsion and bending*. eng. Groningen, 1953.

List of Figures

List of Tables

10   Appendix A

10.1   Mathematical preliminaries of stress field around notch tip

The stress field of an open notch, which becomes a V-crack with a radius of zero, is to be mathematically determined under plane stress-strain conditions. With Kolosoff-Muskhelishvili's [92] method the following analytical potential functions is used:

$$\varphi(z) = az^\lambda, \qquad \psi(z) = bz^\lambda + cz^\mu \tag{74}$$

Where coefficients a, b and c are complex, exponents λ and μ are real, with $\lambda > \mu$ within the hypothesis. When the term cz^μ is neglected in the analysis of open cracks, we get the Williams' solution.
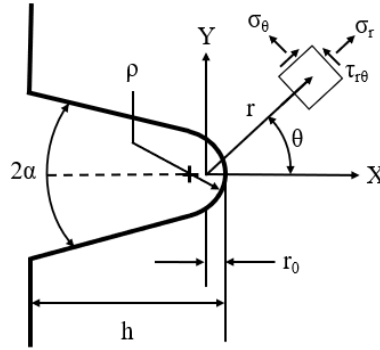

Figure 10.1: Coordinate system for the notch system with symbols used for the stress field components

With the conditions already stated, the polar components result in the stresses:

$$\sigma_\theta = \lambda r^{\lambda-1}[a_1(1-\lambda)cos(1-\lambda)\theta + a_2(1+\lambda)sin(1-\lambda)\theta$$
$$+b_1cos(1+\lambda)\theta - b_2sin(1+\lambda)\theta]$$
$$+\mu r^{\mu-1}[c_1cos(1+\mu)\theta - c_2sin(1+\mu)\theta],$$

$$\sigma_r = \lambda r^{\lambda-1}[a_1(3-\lambda)cos(1-\lambda)\theta + a_2(3+\lambda)sin(1-\lambda)\theta$$
$$-b_1cos(1+\lambda)\theta + b_2sin(1+\lambda)\theta] \tag{75}$$
$$+\mu r^{\mu-1}[-c_1cos(1+\mu)\theta + c_2sin(1+\mu)\theta],$$

$$\tau_{r\theta} = \lambda r^{\lambda-1}[a_1(1-\lambda)sin(1-\lambda)\theta - a_2(1-\lambda)cos(1-\lambda)\theta$$
$$+b_1sin(1+\lambda)\theta + b_2cos(1+\lambda)\theta]$$
$$+\mu r^{\mu-1}[c_1sin(1+\mu)\theta - c_2cos(1+\mu)\theta],$$

The real parameters of (75), λ and μ, as well as the complex components of a, b and c must be evaluated with appropriate boundary conditions. An auxiliary coordinate system as seen in figure (10.2), is useful in the means of imposing the boundary conditions.
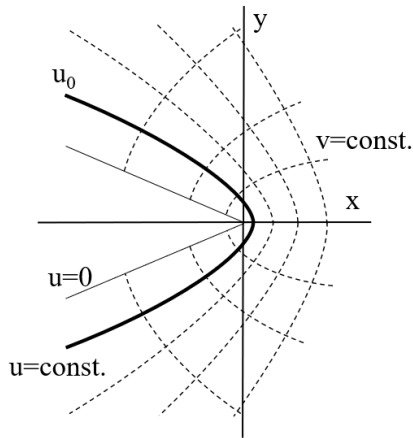
Figure 10.2: An auxiliary coordinate system, with curvilinear coordinates (u,v).

The analytical link between the two coordinate systems is:

$$x + iy = re^{i\theta} = z = w^q = (u + iv)^q \tag{76}$$

The parametric curve corresponding to the condition, $u = 0$, of the curvilinear system, describes a sharp angle equal to 2α in the (x,y) system with:

$$2\alpha = \pi(2 - q) \tag{77}$$

With the free edge of the of a generic smooth notch corresponding to $u = u_0$, give a radius of curvature in correspondence with the abscissa axis with $r_0 = u_0^q$ which equals to:

$$q = \frac{q \cdot u_0^q}{q - 1} = \frac{q \cdot r_0}{q - 1} \tag{78}$$

This radius of curvature is equal to the notch radius. When $q = 2$ the origin of the coordinate system is centred at half of the notch radius $r_0 = \frac{\rho}{2}$ behind the notch tip.
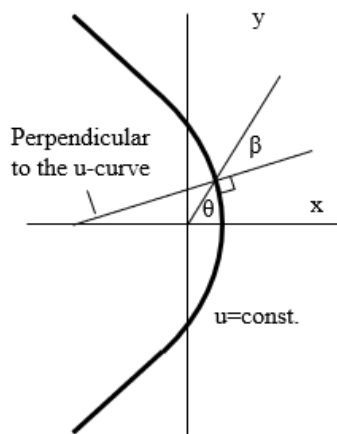

Figure 10.3: The angle (β) between polar and curvilinear systems.

The components of the stress field in the (u,v) curvilinear system can be derived from equation (75) by imposing the local rotation of the reference system, with the angle between the principal directions of the polar and curvilinear systems being $\beta = -\frac{\theta}{q}$, see figure (10.3).

$$\sigma_u = \frac{1}{2}(\sigma_r + \sigma_\theta) + \frac{1}{2}(\sigma_r - \sigma_\theta)\cos\frac{2\theta}{q} - \tau_{r\theta}\sin\frac{2\theta}{q},$$

$$\sigma_v = \frac{1}{2}(\sigma_r + \sigma_\theta) - \frac{1}{2}(\sigma_r - \sigma_\theta)\cos\frac{2\theta}{q} + \tau_{r\theta}\sin\frac{2\theta}{q}, \qquad (79)$$

$$\tau_{uv} = \frac{1}{2}(\sigma_r - \sigma_\theta)\sin\frac{2\theta}{q} + \tau_{r\theta}\cos\frac{2\theta}{q}.$$

The boundary conditions below should be fixed along the free edge of the notch:

$$(\sigma_u)_{u=u_0} = 0, \quad (\tau_{u,v})_{u=u_0} = 0. \qquad (80)$$

However these BC can not be satisfied all along the free edge of the notch, because of a small number of free parameters chosen for the definition of the stress functions. To overcome this problem it should be noted that the BC of (80) should be satisfied within the necessary distance away from the tip, where v have no influence. The stress field should be accurate close to the notch root, giving the two terms of the series expansions along the free edge, related to the stresses σ_u and τ_{uv}, a value of zero. With these considerations the general BC of σ_u is modified to be:

$$(\sigma_u)_{\substack{v \gg u_0 \\ u=u_0}} = 0 \rightarrow \lim_{\substack{r\to\infty \\ \theta\to\pm q\pi/2}} (r^{1-\lambda}\sigma_\theta) = 0, \qquad (81)$$

$$(\sigma_u)_{\substack{u=u_0 \\ v=0}} = (\sigma_r)_{\substack{r=u_0^q \\ \theta=0}} = 0, \qquad (82)$$

$$\left(\frac{\partial\sigma_u}{\partial v}\right)_{\substack{u=u_0 \\ v=0}} = 0 \rightarrow \left(\frac{\partial\sigma_r}{\partial\theta}\right)_{\substack{r=u_0^q \\ \theta=0}} - \frac{2}{q}(\tau_{r\theta})_{\substack{r=u_0^q \\ \theta=0}} = \left(\frac{\partial\sigma_r}{\partial\theta}\right)_{\substack{r=u_0^q \\ \theta=0}} = 0. \qquad (83)$$

With three similar BC's for τ_{uv}. It is important, due to the small numbers of BC's, that the actual trend of such components along the free edge is verified in order to state how approximate the solution will be.

10.1.1 Evaluation of parameters and constants

With equation (81) for σ_u and the similar one for τ_{uv}, gives the same conditions already proposed by William's for the sharp V-cracks, which is shown below.

$$\begin{bmatrix} (1+\lambda)\cos(1-\lambda)\frac{q\pi}{2} & \cos(1+\lambda)\frac{q\pi}{2} & 0 & 0 \\ (1-\lambda)\sin(1-\lambda)\frac{q\pi}{2} & \sin(1+\lambda)\frac{q\pi}{2} & (1+\lambda)\sin(1-\lambda)\frac{q\pi}{2} & -\sin(1+\lambda)\frac{q\pi}{2} \\ 0 & 0 & (1-\lambda)\cos(1-\lambda)\frac{q\pi}{2} & -\cos(1+\lambda)\frac{q\pi}{2} \end{bmatrix}$$

$$\begin{Bmatrix} a_1 \\ b_1 \\ a_2 \\ b_2 \end{Bmatrix} = \begin{Bmatrix} 0 \\ 0 \\ 0 \\ 0 \end{Bmatrix}. \qquad (84)$$

Only when the determinants are zero, we get nontrivial solutions, which leads to the following equations to determine λ:

$$\sin(\lambda_1 q\pi) + \lambda_1 \sin(q\pi) = 0 \quad \text{first determinant, Mode I fracture,} \quad (85)$$

$$\sin(\lambda_2 q\pi) - \lambda_2 \sin(q\pi) = 0 \quad \text{second determinant, Mode II fracture.} \quad (86)$$

Equations (85) and (86) gives multiple solutions or eigenvalues, n. The values of each constant are given by (87, 88)

$$
\begin{aligned}
b_{1n} &= -a_{1n}(1 + \lambda_{1n})\frac{\cos(1 - \lambda_{1n})\frac{q\pi}{2}}{\cos(1 + \lambda_{1n}\frac{q\pi}{2}} \\
&= -a_{1n}(1 - \lambda_{1n})\frac{\sin(1 - \lambda_{1n})\frac{q\pi}{2}}{\sin(1 + \lambda_{1n})\frac{q\pi}{2}} \\
&= a_{1n}(1 - \lambda_{1n})X_{1n}
\end{aligned}
\quad (87)
$$

$$
\begin{aligned}
b_{2n} &= a_{2n}(1 + \lambda_{2n})\frac{\cos(1 - \lambda_{2n})\frac{q\pi}{2}}{\cos(1 + \lambda_{2n})\frac{q\pi}{2}} \\
&= a_{2n}(1 - \lambda_{2n})\frac{\sin(1 - \lambda_{2n})\frac{q\pi}{2}}{\sin(1 + \lambda_{2n})\frac{q\pi}{2}} \\
&= -a_{2n}(1 - \lambda_{2n})X_{2n}
\end{aligned}
\quad (88)
$$

With X_{ik} equal to:

$$X_{ik} = -\frac{\sin(1 - \lambda_{ik})\frac{q\pi}{2}}{\sin(1 + \lambda_{ik})\frac{q\pi}{2}} \quad (89)$$

$$
= \lambda_{1n}a_{1n}\frac{\mu_{1n}r_0^{\mu-\lambda}\left[\frac{1}{\frac{1}{q}-(1+\mu_{1n})}\right]c_{1n}}{\left[(1-\lambda_{1n})^2 - \frac{(1+\lambda_{1n})}{q}\right] + X_{1n}(1-\lambda_{1n})[(1+\lambda_{1n})-\frac{1}{q}]}\frac{(3-\lambda_{1n})-X_{1n}(1-\lambda_{1n})}{} \quad (90)
$$

$$
= \lambda_{1n}a_{1n}\frac{\mu_{1n}r_0^{\mu-\lambda}\left[\frac{1}{\frac{1}{q}-(1+\mu_{1n})}\right]c_{1n}}{\left[(1-\lambda_{1n})^2 - \frac{(1+\lambda_{1n})}{q}\right] + X_{1n}(1-\lambda_{1n})\left[(1+\lambda_{1n})-\frac{1}{q}\right]}\frac{(3-\lambda_{1n})-X_{1n}(1-\lambda_{1n})}{} \quad (91)
$$

Values for the parameters μ and of the real and imaginary c, can be obtained for both modes by imposing that the previous two equations have nontrivial solutions, giving:

$$\mu_{1n} = \frac{1}{q} - \left\{\frac{\left[(1-\lambda_{1n})^2 - \frac{(1-\lambda_{1n})}{q}\right] + X_{1n}(1-\lambda_{1n})\left[(1+\lambda_{1n})-\frac{1}{q}\right]}{(3-\lambda_{1n})-X_{1n}(1-\lambda_{1n})}\right\} - 1, \quad (92)$$

$$\mu_{2n} = -\left\{\frac{[(3-\lambda_{2n})(1-\lambda_{2n})] - X_{2n}(1-\lambda_{2n})^2}{(1-\lambda_{2n}) + X_{2n}(1-\lambda_{2n})}\right\} - 1, \quad (93)$$

$$c_{1n} = \frac{\lambda_{1n}}{\mu_{1n}} r_0^{\lambda_{1n}-\mu_{1n}} a_{1n}[(3-\lambda_{1n}) - X_{1n}(1-\lambda_{1n})], \tag{94}$$

$$c_{2n} = \frac{\lambda_{2n}}{\mu_{2n}} r_0^{\lambda_{2n}-\mu_{2n}} a_{2n}[(3-\lambda_{2n}) - X_{2n}(1-\lambda_{2n})]. \tag{95}$$

Figure 10.4: A plot of exponents versus the notch opening angle, 2α.

Finally it is possible with a general formulation of the stress components. For tension, Mode I the stress field is:

$$
\begin{Bmatrix} \sigma_\theta \\ \sigma_r \\ \tau_{r\theta} \end{Bmatrix} = \lambda_1 r^{\lambda_1-1} a_1 \left\{ \left[\begin{Bmatrix} (1+\lambda_1)\cos(1-\lambda_1)\theta \\ (3-\lambda_1)\cos(1-\lambda_1)\theta \\ (1-\lambda_1)\cos(1-\lambda_1)\theta \end{Bmatrix} \right. \right. \\
+ X_1(1-\lambda_1) \begin{Bmatrix} \cos(1+\lambda_1)\theta \\ -\cos(1+\lambda_1)\theta \\ \sin(1+\lambda_1)\theta \end{Bmatrix} \\
\left. + \left(\frac{r}{r_0}\right)^{(\mu_1-\lambda_1)} [(3-\lambda_1) - X_1(1-\lambda_1)] \begin{Bmatrix} \cos(1+\mu_1)\theta \\ -\cos(1+\mu_1)\theta \\ \sin(1+\mu_1)\theta \end{Bmatrix} \right. \tag{96}
$$

And for Mode II:

$$
\begin{Bmatrix} \sigma_\theta \\ \sigma_r \\ \tau_{r\theta} \end{Bmatrix} = \lambda_2 r^{\lambda_2-1} a_2 \left\{ \left[\begin{Bmatrix} (1+\lambda_2)\cos(1-\lambda_2)\theta \\ (3-\lambda_2)\cos(1-\lambda_2)\theta \\ (1-\lambda_2)\cos(1-\lambda_2)\theta \end{Bmatrix} \right. \right. \\
+ X_2(1+\lambda_2) \begin{Bmatrix} \cos(1+\lambda_2)\theta \\ -\sin(1+\lambda_2)\theta \\ \sin(1+\lambda_2)\theta \end{Bmatrix} \\
\left. - \left(\frac{r}{r_0}\right)^{(\mu_2-\lambda_2)} [(1-\lambda_2) + X_2(1+\lambda_2)] \begin{Bmatrix} \cos(1+\mu_2)\theta \\ -\sin(1+\mu_2)\theta \\ \sin(1+\mu_2)\theta \end{Bmatrix} \right. \tag{97}
$$